Available online at www.sciencedirect.com
ScienceDirect
Comput. Methods Appl. Mech. Engrg. 392 (2022) 114728
Computer methods in applied mechanics and engineering
www.elsevier.com/locate/cma

Fluid–structure interaction approach with smoothed particle hydrodynamics and particle–spring systems

Alessandra Monteleone[a], Guido Borino[b], Enrico Napoli[b], Gaetano Burriesci[a,c,*]

[a] *Bioengineering Unit, Ri.MED Foundation, Palermo, Italy*
[b] *Università degli Studi di Palermo, Dipartimento di Ingegneria, Viale delle Scienze, 90128 Palermo, Italy*
[c] *UCL Mechanical Engineering, University College London, London, United Kingdom*

Received 11 June 2021; received in revised form 3 February 2022; accepted 3 February 2022
Available online 23 February 2022

Abstract

This paper presents a novel three-dimensional fluid–structure interaction (FSI) approach, where the meshless smoothed particle hydrodynamics (SPH) method is used to simulate the motion of incompressible fluid flows, whilst structures are represented by a simplified approach based on particle–spring systems. The proposed FSI technique allows to use independent spatial–temporal resolutions for the fluid and structural computational domains. The particle–spring elastic constants are calibrated and relationships with the mechanical material properties, Young's modulus and Poisson's ratio, are determined. Fluid and structure computational domains are separated by interfaces made of triangular elements whose position is updated during the simulation following the structural deformation. The coupling of the two media at the fluid–structure interfaces is handled by the introduction of solid and fluid boundary particles. This approach, automatically and without introducing further complexity, avoids the penetration of fluid particles into the solid domain. The efficiency and accuracy and the present method are validated with analytical/benchmark solutions from the literature.

Keywords: Smoothed particle hydrodynamics (SPH); Fluid–structure interaction (FSI); Particle–spring systems; Particle-based FSI; FSI benchmark

1. Introduction

Fluid–structure interaction (FSI) is a key factor in many multi-physics problems, particularly in cardiovascular biomechanics. In this framework, modeling pulsatile blood flow within complex domains, such as deformable vessels or heart valves, is challenging and requires advanced FSI strategies. On one hand the walls move and deform under the mechanical actions exerted by the blood, on the other hand the structure movement consequently influences the haemodynamics. As a result, a two-way interaction between the fluid and the deformable structure occurs at the interface separating the two phases, where a suitable and sufficiently accurate matching solution must be imposed in a consistent and physical manner.

Eulerian formulations are traditionally adopted for the fluid modeling, whilst structures are commonly more conveniently described through Lagrangian approaches. The matching of the two media is usually achieved employing Arbitrary-Lagrangian–Eulerian (ALE) techniques [1–4] or Immersed Boundary (IB) strategies [5].

* Corresponding author at: UCL Mechanical Engineering, University College London, London, United Kingdom.
E-mail address: g.burriesci@ucl.ac.uk (G. Burriesci).

https://doi.org/10.1016/j.cma.2022.114728

An alternative FSI approach is based on the description of both fluid and structure phases through a Lagrangian formulation. Fully-Lagrangian solvers can lead to an efficient and consistent imposition of fluid–structure interface boundary conditions, especially when large deformations are considered, thus avoiding mesh distorsion issues at the FSI interface [6–9].

In the framework of the Lagrangian particle method, smoothed particle hydrodynamics (SPH) has recently emerged as one of the most efficient mesh-free techniques for simulating fluid flows [10]. Originally developed in astrophysics by Lucy [11] and Gingold and Monaghan [12], it was more recently successfully employed in a wide range of problems in engineering and sciences [13], including several FSI applications [14]. As a mesh-free particle method, SPH conveniently treats multi-phase flows, highly complex geometries and large deformations, efficiently capturing rapidly moving interfaces; therefore, complex FSI problems can be reliably simulated. Exploiting these advantages, a considerable number of SPH-based techniques for solving FSI problems were developed in the past. Several studies have adopted a partitioned approach, where SPH is used to solve the fluid domain, whilst a separate solver based on a different numerical method is employed to analyze the solid domain. Although partitioned approaches allow the selection of specialised solvers for each domain, ensuring the coherent transfer of information (load, displacement and velocities) through the interface between the two solvers is a very challenging task, especially when the two solvers are very different in formulation. This is the case when coupling the SPH meshless method with a mesh-based one, such as the finite element method (FEM), which is the most established approach for structural dynamic simulations [15–21]. Further complexity is introduced by the potentially large element distortion that characterizes FEM methods, and the need to enforce appropriate master–slave contact algorithms between the two solvers, which require the determination and application of contact forces to prevent the fluid particles from penetrating into the solid domain [15,16]. Ghost particles schemes were introduced by other authors in the attempt to better address these issues [20,21]. An alternative approach was proposed by Sun et al. [22], based on coupling of a δ-SPH scheme for complex multi-phase flows and a Total-Lagrangian Particle solver for elastic structures, for the modeling of violent FSI problems. SPH was also integrated with the element bending group (EBG) method for modeling the interaction between viscous flows and membrane structures. The SPH-EBG coupling approach was originally proposed by Hosseini and Feng [23] to model the deformation of floating red blood cells, represented by a set of discrete particles connected by nonlinear springs. The method was successively extended by Yang et al. [24] to study the interaction between free-surface flows and flexible structures. However, the method has been mostly applied to two-dimensional applications. Other authors proposed monolithic approaches, where the governing equations for fluid flow and structure displacements are solved simultaneously by a single SPH solver, both in the weakly-compressible SPH -WCSPH- [25,26] and the truly incompressible -ISPH- [27,28] schemes. Morikawa and Asai [29] proposed a two-way FSI technique by coupling a total Lagrangian SPH method enforced by the Jameson–Schmidt–Turkel stabilization procedure [30], for elastic solid bodies, and the fully explicit incompressible SPH scheme [31] for the fluid domain. Their coupling technique could avoid penetration of fluid particles into the solid body by means of a non-penetration numerical algorithm.

A different FSI approach, based on a combination of lattice Boltzmann and lattice spring models (LBM and LSM, respectively), was proposed by Buxton et al. [32] to simulate the breathing-mode behavior of an elastic shell. The lattice spring model consisted of a network of harmonic springs that connected regularly spaced mass points. The basic model is restricted to the simulation of solid materials characterized by a Poisson's ratio equal to 0.25, and more complex many-body interactions need to be introduced to vary this value [32]. SPH was also successfully coupled with discontinuous approaches based on the description of the solid phase through particles connected via spring-like forces [33–35]. However, most of the discontinuous model, such as LSM or the discrete element method (DEM), cannot model solid body of arbitrary Poisson's ratio. For example, in the FSI models of Tan and Chen [33],Wu et al. [34], which are based on coupling SPH with DEM, the Poisson's ratio of the solid material needs to be kept below certain critical values in order to guarantee a non-negative spring stiffness value. In this framework, Ng et al. [36] proposed a different approach based on coupling SPH with Volume Compensated Particle Method (SPH-VCPM) where axial interactions between solid particles are introduced to model large Poisson's ratios.

A common limitation of SPH-based FSI approaches is that the spatial and temporal resolutions are usually not independent for the fluid and solid computational domains. In particular, in FSI techniques where SPH formulation is used for representing both fluid, and solid dynamics, a uniform particle spacing is generally used, despite the need to implement multi-resolution schemes is widely recognised [27–29]. In fact, a constant resolution approach can result too expansive in applications when the fluid and solid domains are characterized by different scale lengths,

as the finest resolution required for each of the two domains needs to be applied to the whole system. In this context, Zhang et al. [26] recently proposed a multi-resolution approach, where spatial discretisation is applied with different resolutions to the fluid and structure. Yet, the fluid and solid discretization are not completely untied, and a coarser resolution is required for the fluid. Therefore, this approach is not accurate in applications where the fluid domain needs higher spatial resolution, for example when near wall flow structures need to be captured or fluids are highly viscous non-Newtonian. The problem of the decoupling of fluid and solid particle dimensions remains a significant issue even when SPH is coupled with other discontinuous approaches for the description of the solid phase. In this context, a single particle size is typically employed for the solid and fluid domains [35,36]. The use of different resolutions for the two domains introduces a number of further limitations. This is, for example, the case of SPH-DEM approaches, where the SPH *smoothing length* of the fluid needs to be sufficiently larger than the solid particle diameter [33,34]. In order to overcome the computational efforts deriving from a unique particle dimension for the fluid and structural domains, hardware acceleration platforms, such as graphics processing units (GPUs) have become a valid and interesting strategy. Recently, O'Connor and Rogers [37] presented a numerical model based on a unified SPH framework for free-surface flows with flexible fluid–structure interaction, accelerated with a graphics processing unit (GPU). The method, implemented within the open-source SPH code DualSPHysics for weakly-compressible flows, involved a Total Lagrangian model to solve the structural dynamics and did not require the geometrical knowledge of the fluid–structure interface.

This paper presents a new three-dimensional FSI approach, based on the coupling between ISPH for the fluid flow dynamics and a particle–spring model for the structure movements. The proposed approach is mainly focused on the impact of the structural deformation on the fluid dynamics. Therefore, a simplified description for the solid phase is chosen, where structures are represented by a finite number of moving particles regularly spaced, which are connected via spring-links, similarly to the LSM. A procedure to calibrate the spring elastic coefficients is proposed and practical relationships relating the spring constants and the material mechanical properties are determined and described. Differently from the common discontinuous approaches, the introduction of these relationships allows to set a wide range of values for the Poisson's ratio of the material. The proposed method allows to use different spatial and temporal discretization for the fluid and the structure. This is a major advantage in a number of cardiovascular studies, where the solid components often consist of thin structures composed of multiple layers with different material properties and highly nonlinear constitutive laws (e.g. vessel walls, heart valve leaflets, etc.).

A new efficient and easy treatment of the interface separating the fluid and solid computational domains is proposed. The interface is identified by boundary nodes that follow the solid deformation and apply the forces exerted by the fluid on the structure. On the other hand, appropriate coupling conditions are imposed at the fluid wall through the mirror particle procedure. This approach, automatically and without introducing further complexity, avoids the penetration of fluid particles into the solid domain. This is a relevant issue of FSI partitioned approaches, typically addressed by enforcing complex non-penetration numerical algorithms [15,16,29].

Due to its simplicity, the method is straightforwardly implementable and extendable in a WCSPH scheme as well. Moreover, since the dynamics of both fluid and structure are modeled using particle-based methods, the proposed FSI method can easily be parallelized on multiple Central and/or Graphical Processor Unit (CPU and GPU, respectively) architectures. The model is validated through the Womersley's analytical solution for pulsatile flow in a cylindrical vessel [38] and the benchmark computational test proposed by Turek and Hron [39].

The presented FSI approach is developed and implemented in the open-source *PANORMUS* (PArallel Numerical Open-souRce Model for Unsteady flow Simulations) package, distributed under the terms of the *GNU General Public License* [40], which contains a SPH solver for incompressible flows [41].

2. Smoothed particle hydrodynamics

2.1. Basic SPH formulation

In the present approach, the fluid domain is modeled by means of SPH numerical method. SPH is based on the definition of a *kernel function* W, with *smoothing length* h_f, which allows to express the generic hydrodynamic variable a at point $\mathbf{x}$ through the convolution integral

$$\langle a(\mathbf{x})\rangle = \int_D a(\mathbf{x}')\, W(\mathbf{x}-\mathbf{x}', h_f) d\mathbf{x}' \tag{1}$$

where D is the fluid domain and $W(\mathbf{x}-\mathbf{x}', h_f)$ is the *kernel function* value depending on the distance between $\mathbf{x}$ and $\mathbf{x}'$. The *kernel function* takes null values for distances $|\mathbf{x}-\mathbf{x}'|$ larger than kh_f, where k is a constant whose value depends on the shape of the specified *kernel function*. In this paper the *Wendland* function [42] is used (where $k=2$).

In the discretized form of the scheme, the fluid domain is represented by a finite number of fluid particles which, while moving satisfying Navier–Stokes equations, carry fluid properties such as position, mass, velocity, pressure, etc. Each fluid particle i has a *support domain*, indicated as Ω_i, which includes all the neighboring j particles having a distance d_{ij} less than kh_f from the i particle. In the particle approximation, the convolution integral equation (1) for the generic i particle can be approximated as the summation over the N_i particles lying into its *support domain* Ω_i

$$a_i = \sum_{j=1}^{N_i} \frac{m_j}{\rho_j} a(\mathbf{x}_j)\ W_{ij} \tag{2}$$

where $\mathbf{x}_j$ is the jth particle position, $a_i \approx \langle a(\mathbf{x}_i)\rangle$, m_j and ρ_j are the mass and density of the neighboring particle j, respectively, and $W_{ij} = W(\mathbf{x}_i - \mathbf{x}_j, kh_f)$ is the value of the *kernel function* at the distance d_{ij} between particles i and j.

In this paper, in the starting reference configuration the fluid particles were arranged at an isotropic initial distance Δx equal to $kh_f/2$ (where $k=2$ for the Wendland function). This leads to a ratio $h_f/\Delta x = 1$. Although this is slightly below the values commonly used in the literature, which typically range between 1.2 and 1.33 [43–48], it has been shown in previous works to provide good accuracy in the solution [41,49–51], whilst limiting the number of *mirror* particles to be generated (this is a major advantage when the boundaries have a heavy influence and the ratio between the domain surface and volume is large).

First derivatives of a are obtained through the derivative of the *kernel function* using the *Basic* or *Difference Gradient Approximation* (Eqs. (3) and (4), respectively)

$$\left.\frac{\partial a}{\partial x}\right|_i = -\sum_{j=1}^{N_i} \frac{m_j}{\rho_j} a_j \left.\frac{\partial W_{ij}}{\partial x}\right|_i \tag{3}$$

$$\left.\frac{\partial a}{\partial x}\right|_i = -\sum_{j=1}^{N_i} \frac{m_j}{\rho_j} \left(a_i - a_j\right) \left.\frac{\partial W_{ij}}{\partial x}\right|_i \tag{4}$$

while the Laplacian operator at the position of the ith particle is expressed by the Morris' formula [52]

$$\nabla^2 a\big|_i = \sum_{j=1}^{N_i} 2\frac{m_j}{\rho_j} \frac{\left(\mathbf{x}_i - \mathbf{x}_j\right)\cdot\nabla W_{ij}}{d_{ij}^2} \left(a_i - a_j\right) \tag{5}$$

where the symbol '$\cdot$' indicates the scalar product and ∇W_{ij} is the gradient of the *kernel function*.

2.2. Boundary treatment

Additional particles, named *mirror* particles in the following, are generated at solid walls to impose suitable boundary conditions. Specifically, these particles are introduced through the mirroring, with respect to the solid walls, of the particles having distances no larger than kh_f from the boundaries. In order to simplify the mirroring procedure, boundaries are discretized into triangles, so as to ease the identification of normal directions (they lie in planes) and the distance from the particles to be mirrored. For more details regarding the mirror particle procedure, see among others [41]. In the proposed approach, fluid and solid computational domains are separated by FSI interfaces through which the share of information (loads, displacements and velocities) occurs. The FSI interfaces overlap the existing fluid boundaries in contact with the structure. Therefore, these boundaries, which are fixed for rigid walls, become moving boundaries for the fluid when FSI conditions are imposed, without requiring additional building of interface boundary surfaces. As for fixed solid walls, virtual particles are introduced through the mirroring of the fluid particles close to the boundary. When the no-slip boundary condition is imposed at the wall, the velocity of the *mirror* is set equal to $2\mathbf{u}_i - \mathbf{u}_p$, where $\mathbf{u}_p$ is the velocity of the effective particle generating

the *mirror* particle and $\mathbf{u}_i$ is the velocity of the triangle through which the *mirror* has been generated. The velocity $\mathbf{u}_i$ is null for fixed walls and is equal to the rate of displacement of the solid when FSI condition is considered.

Inflow and outflow boundaries are treated in a similar way, introducing additional particles to impose the required pressure and velocity boundary conditions. Moreover, the particles leaving or entering the domain through open boundaries are dealt in an efficient way, satisfying the global mass conservation requirement. The procedure is described in detail in [50].

2.3. ISPH procedure

In the existing SPH solver contained in the *PANORMUS* software, a *fractional-step* procedure is used to solve the momentum and continuity equations for incompressible flows [41]. The procedure allows to obtain the velocity $\mathbf{u}^{r+1}$ at the updated $(r+1)$th time step as the sum of the non-solenoidal intermediate velocity $\mathbf{u}^*$ and the corrective velocity $\mathbf{u}^c$.

In the *predictor-step*, $\mathbf{u}^*$ is obtained solving the momentum equations without the pressure gradient term

$$\frac{\mathbf{u}_i^* - \mathbf{u}_i^r}{\Delta t_f} = \left[\frac{3}{2}\mathbf{D}_i^r - \frac{1}{2}\mathbf{D}_i^{r-1}\right] + \mathbf{g} \tag{6}$$

where Δt_f is the time step of the fluid computational model, $\mathbf{g}$ is the mass force per unit mass, $\mathbf{u}_i^r$ is the i particle velocity at the rth time step and $\mathbf{D}$ is the diffusive term expressed through a second-order Adams–Bashforth scheme. By using Eq. (5), the diffusive term for the i particle can be expressed as

$$\mathbf{D}_i = \sum_{j=1}^{N_i} (\nu_i + \nu_j)\frac{m_j}{\rho_j}\frac{(\mathbf{x}_i - \mathbf{x}_j)\cdot\nabla W_{ij}}{d_{ij}^2}(\mathbf{u}_i - \mathbf{u}_j) \tag{7}$$

where ν_i is the kinematic viscosity of the i particle.

The corrective velocity field $\mathbf{u}^c$ is irrotational and its potential $\psi\,\Delta t_f$ is obtained solving the Pressure Poisson Equation (PPE)

$$\nabla^2\psi = -\frac{\nabla\cdot\mathbf{u}^*}{\Delta t_f} \tag{8}$$

which, in the SPH approximation, reads as

$$\sum_{j=1}^{N_i} 2\frac{m_j}{\rho_j}\frac{(\mathbf{x}_i^r - \mathbf{x}_j^r)\cdot\nabla W_{ij}}{d_{ij}^2}(\psi_i - \psi_j) = \frac{1}{\Delta t_f}\sum_{j=1}^{N_i}\frac{m_j}{\rho_j}(\mathbf{u}_i^* - \mathbf{u}_j^*)\cdot\nabla W_{ij} \tag{9}$$

Eq. (9) is solved using *Neumann* boundary conditions at the solid walls

$$\left.\frac{\partial\psi}{\partial n}\right|_i = \frac{u_{in}^{r+1} - u_{in}^*}{\Delta t_f} \tag{10}$$

where n is the direction normal to the boundary, u_{in}^{r+1} and u_{in}^* are the normal components of the assigned wall velocity and intermediate velocity, respectively, at the intersection point between the boundary and the normal line starting from the i particle. It should be noted that u_{in}^{r+1} is equal to zero for fixed walls, whilst it is equal to the FSI interface velocity in the proposed FSI approach. On the other hand, an extrapolation from the interior of the domain is used to obtain the intermediate velocity u_{in}^* [53]. The discretized Pressure Poisson equations (9) are solved using for the whole fluid domain a single equation system whose solution is obtained through a pre-conditioned BicGStab algorithm [54].

In the *corrector-step*, the corrective velocity $\mathbf{u}_i^c$ and the updated solenoidal velocity $\mathbf{u}_i^{r+1}$ of the i particle can be obtained as

$$\mathbf{u}_i^c = \nabla\psi\,\Delta t_f \approx -\Delta t_f \sum_{j=1}^{N_i}\frac{m_j}{\rho_j}\left(\psi_i - \psi_j\right)\nabla W_{ij} \tag{11}$$

The updated velocity field is thus obtained as sum of the intermediate and corrective velocities

$$\mathbf{u}_i^{r+1} = \mathbf{u}_i^* + \mathbf{u}_i^c \tag{12}$$

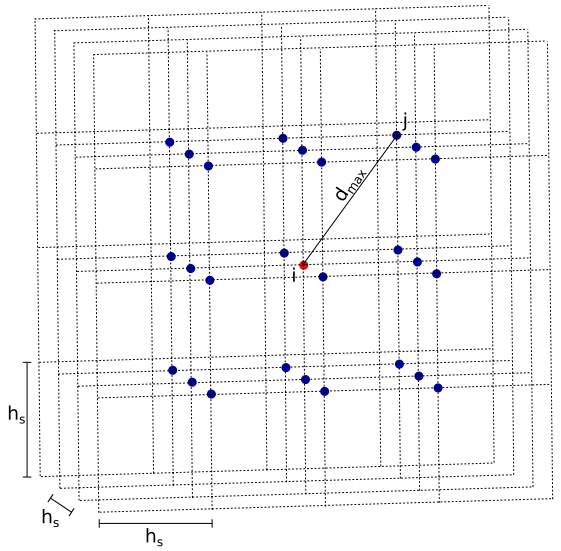

Fig. 1. 3D sketch of the solid particles in the reference configuration. Light blue dots: solid particles; red dot: i solid particle; blue dots: solid particles neighbor to i ($d_{max} \leq \sqrt{3}\ h_s$).

The position $\mathbf{x}_i^{r+1}$ of particle i can be updated using the mean velocity between the rth and $(r+1)$th time instants

$$\mathbf{x}_i^{r+1} = \mathbf{x}_i^r + \frac{\mathbf{u}_i^{r+1} + \mathbf{u}_i^r}{2} \Delta t_f \tag{13}$$

3. The proposed numerical model

3.1. Solid model

As mentioned in the introduction, the proposed approach is aimed at improving the accuracy of fluid dynamic analyzes in cases where the compliance of the structure can have a relevant effect on the fluid motion. Hence, implementing a complex formulation able to capture the complex constitutive laws characterizing the soft tissues mechanics is out of the current scope. Therefore, a simplified technique was employed for the representation of the solid, based on particle–spring systems. Specifically, the solid is represented by a finite number of particles having a constant distance h_s in the reference configuration (Fig. 1). Each solid particle is linked to the neighboring particles of the same phase at a distance equal or lower than $\sqrt{3}\,h_s$. As a result, a solid particle internal to the domain has 26 or 8 neighboring particles in the $3D$ and $2D$ approximations, respectively. In Fig. 1, the generic solid particle i is represented by a red dot, whilst the particles to which i is connected are represented by dark blue dots. The generic solid particle i has associated material properties, such as mass m_i and volume h_s^3 (hence the particle density is $\rho_i = m_i / h_s^3$).

Contrary to the SPH method, in the hypothesis of full integrity of the continuum linear elastic solid phase, the links between solid particles were set not to change in time, so that the particle i maintains the same neighboring particles j for the whole simulation. Each pair $i - j$ of mass points is connected via a spring having an elastic constant k_e. Fig. 2a represents a 2D sketch of the spring system for a generic solid particle i in the reference configuration. The rest distances from i to the j neighboring particles are denoted as $l_{0,ij}$, while in the deformed states they are indicated as l_{ij}.

Under the influence of external actions (*e.g.* imposed loads or displacements) the reference configuration can change (Fig. 2b) and the spring lengths are updated accordingly. The solid structure thus deforms achieving a configuration where these external forces are counterbalanced by opposing internal forces. Consequently, the springs experiencing tension or compression respond by applying forces, attempting to preserve their rest length. Indicating

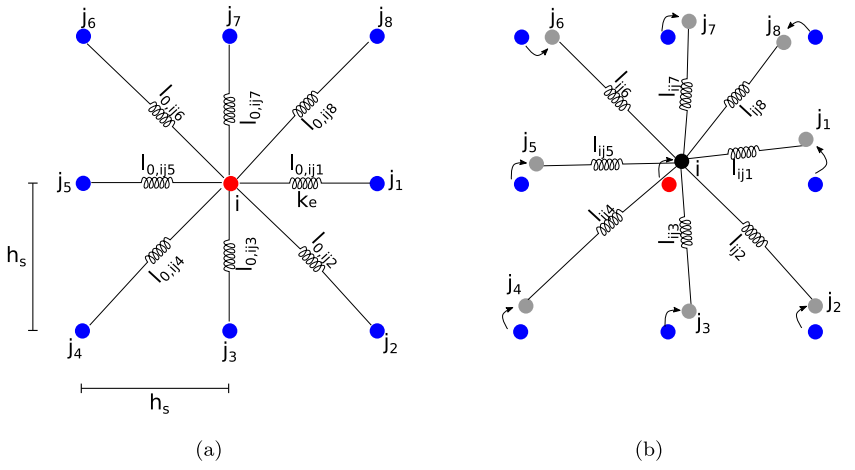

Fig. 2. 2D sketch of the spring system centered at the particle i. (a) reference configuration; (b) deformed configuration. Blue dots: solid particles in reference configuration; red and black dots: i particle in reference and deformed configuration, respectively; blue and gray dots: solid particles neighbor to i in reference and deformed configuration, respectively.

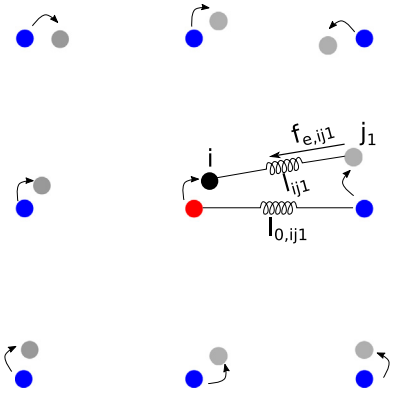

Fig. 3. Elastic force for the generic spring $i - j_1$. Symbols as in Fig. 2.

with l_{ij} the instantaneous updated distances from i to the j neighboring particles, the internal elastic force $f_{ij,e}$ acting on i to restore the initial distance $l_{0,ij}$ (see Fig. 3) can be expressed as

$$\mathbf{f}_{ij,e} = k_e \; h_s \left(l_{0,ij} - l_{ij}\right) \; \hat{\mathbf{x}}_{ij} \tag{14}$$

where $\hat{\mathbf{x}}_{ij} = (\mathbf{x}_i - \mathbf{x}_j)/l_{ij}$ is the unit vector directed from i to j.

Therefore, the total elastic force acting on the generic mass point i ($\mathbf{f}_{i,e}$) is the sum of all the elastic forces generated from all the springs connected to i, whose number is indicated as N_i

$$\mathbf{f}_{i,e} = \sum_{j=1}^{N_i} \mathbf{f}_{ij,e} \tag{15}$$

In order to model the Poisson's effect, a volumetric force $\mathbf{f}_v$ is introduced, which opposes variations in the volume associated with each solid particle. Specifically, the generic solid particle i generates a force, with magnitude w_i, that acts towards all the j particles linked to i. The magnitude w_i is proportional to the difference $\bar{l}_{0,i} - \bar{l}_i$ where $\bar{l}_{0,i}$ and $\bar{l}_i$ are the average distances from i and its neighboring particles in the reference and deformed configurations,

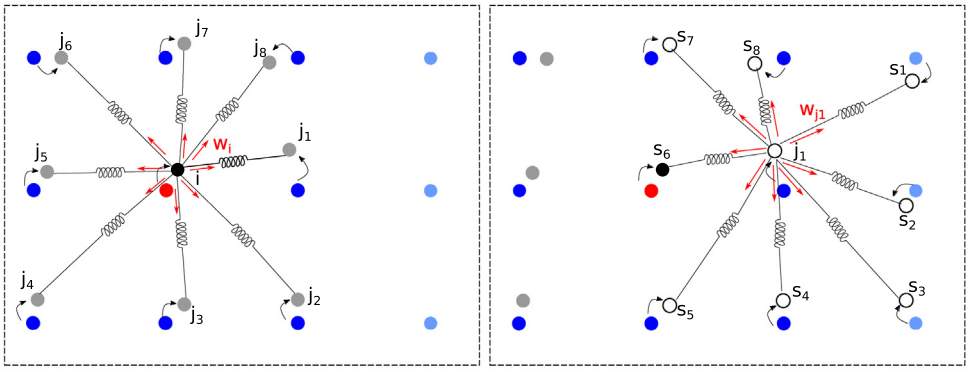

Fig. 4. 2D sketch of the volumetric force determination. Empty black dots: particles neighbor to j_1. Other symbols as in Fig. 2. (a) and (b) forces of magnitude w_i and w_{j1} exerted by the particles i and j_1, respectively, in all the directions to restore their volume.

respectively. This can be expressed as

$$w_i = k_v\ h_s\ \left(\frac{1}{N_i} \sum_{j=1}^{N_i} l_{0,ij} - \frac{1}{N_i} \sum_{j=1}^{N_i} l_{ij} \right) = k_v\ h_s\ \left(\bar{l}_{0,i} - \bar{l}_i \right) \tag{16}$$

where k_v is a coefficient whose value is related to the Poisson's ratio. On the other hand, the magnitude of the volumetric force w_j generated by the generic particle j, neighbor to i, is

$$w_j = k_v\ h_s\ \left(\frac{1}{N_j} \sum_{s=1}^{N_j} l_{0,js} - \frac{1}{N_j} \sum_{s=1}^{N_j} l_{js} \right) = k_v\ h_s\ \left(\bar{l}_{0,j} - \bar{l}_j \right) \tag{17}$$

where N_j is the total number of particles linked to j, and the average distances $\bar{l}_{0,j}$ and $\bar{l}_j$ are calculated considering j and its neighboring particles (indicated with s in the summation). Figs. 4a,b show w_i for the particle i and w_{j1} for the particle j_1 neighbor to i, respectively. Therefore, when considering the equation for the particle i, a further force is added to the elastic force. Considering the pair $i - j$, this force has magnitude equal to w_j and is oriented in the direction of the spring ($\mathbf{f}_{ij,v} = w_j\ \hat{\mathbf{x}}_{ij}$). In order to ensure that the action–reaction principle is satisfied, the magnitude of the volumetric force acting between particle i and j is defined as the mean value between w_i and w_j. Thus, the volumetric force for the spring $i - j$ reads as

$$\mathbf{f}_{ij,v} = \left(\frac{w_i + w_j}{2} \right)\ \hat{\mathbf{x}}_{ij} \tag{18}$$

In Fig. 5a schematic representation of the volumetric forces acting on the particle i is shown.

The determination of the spring coefficients k_e and k_v in relation to the Young's modulus and Poisson's ratio of the material is discussed in detail in Section 4.

In order to impose external loads, boundary nodes, named *skin* nodes in the following, are introduced at the vertices of triangles describing the boundary of the solid phase (represented by red dots in Fig. 6). As it will be described in Section 3.2, the same procedure is used at the FSI interface to share the information (positions, forces and velocities) between fluid and solid computational domains.

When imposing stress loads on the boundary triangles, a corresponding force is associated to the *skin* nodes. Specifically, the stress is converted into force by multiplying it by the surface of the triangle on which it acts. The resulting force is equally reparted on the three *skin* nodes at the triangle vertices. Each *skin* node is associated to the solid particles with distance lower than h_s from it and the *skin* force is thus distributed over these particles (whose number is indicated with n). In particular, as described in Fig. 6, the force of the *skin* node A, which is indicated as $f_{ext,A}$, is reparted between the adjacent internal solid particles (B and C, with $n = 2$ in the figure). Therefore, the force exerted by the *skin* node A towards its neighboring solid particle B and C is equal to $\frac{\mathbf{f}_{ext,A}}{2}$.

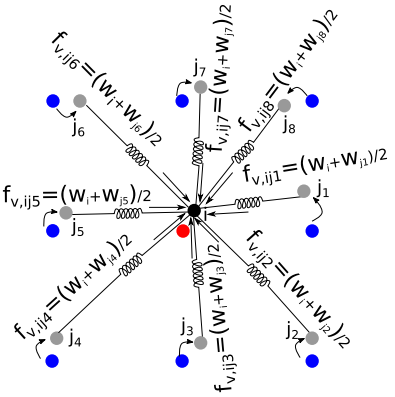

Fig. 5. 2D of the total volumetric force acting on the particle i. Symbols as in Fig. 4.

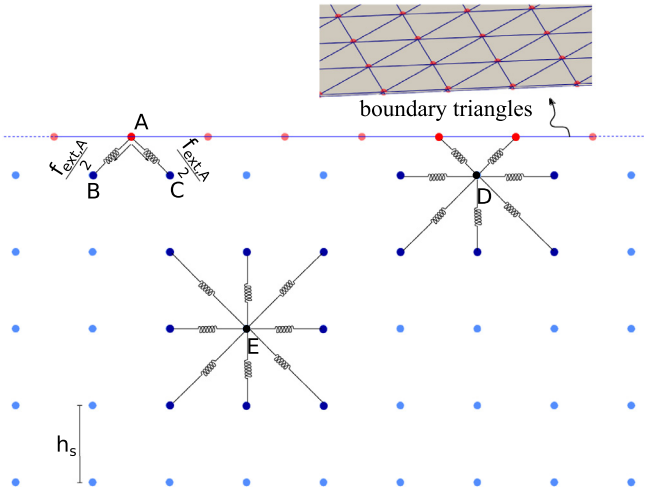

Fig. 6. 2D sketch of the *skin* nodes management. Blue lines: boundary triangles; red dots: *skin* nodes; blue dots: solid particles.

The total force acting on the solid particle i is expressed as

$$\mathbf{f}_{i,tot} = \sum_{j=1}^{N_i} \mathbf{f}_{ij,e} + \sum_{j=1}^{N_i} \mathbf{f}_{ij,v} + \sum_{s=1}^{N_s} \frac{\mathbf{f}_{ext,s}}{n} - \mathbf{f}_{i,d} = \mathbf{f}_{i,e} + \mathbf{f}_{i,v} + \mathbf{f}_{i,ext} - \mathbf{f}_{i,d} \tag{19}$$

where $\mathbf{f}_{i,ext}$ is the sum of the external forces exerted by the s *skin* nodes belonging to the solid structure (whose number is N_s) in the vicinity of i (for example, particle D in Fig. 6 has two *skin* nodes), whilst the external force is zero if i has a distance greater than h_s from the boundary triangles (*e.g.* particle E in the same figure). In Eq. (19), a dissipative force, $\mathbf{f}_{id}$, is included to prevent oscillations of the particles about their equilibrium positions. This force is expressed as a fraction of the velocity $\mathbf{u}_i$ of the i particle

$$\mathbf{f}_{i,d} = \beta \frac{m_i}{\Delta t_s} \mathbf{u}_i \tag{20}$$

where β is a damping coefficient and Δt_s is the time step of the structure computational model.

It should be noted that Eq. (19) remains valid even when a strain is imposed to the material. In this case, the corresponding displacement is transferred from the *skin* nodes to the neighboring internal particles. Eq. (19) is thus simplified removing the third term by the right-and-side ($\mathbf{f}_{i,ext} = 0$).

The dynamics of each solid particle i in a mass–spring network can be described using the Newtonian law of motion

$$\mathbf{f}_{i,tot} = m_i \ \frac{d\mathbf{u}_i}{\Delta t_s} \tag{21}$$

After having calculated the forces, an explicit second-order accurate in time Adams–Bashforth scheme is used to calculate the updated velocity

$$\mathbf{u}_i^{(r+1)} = \mathbf{u}_i^{(r)} + \left(\frac{3}{2}\mathbf{f}_{i,tot}^{(r)} - \frac{1}{2}\ \mathbf{f}_{i,tot}^{(r-1)}\right)\ \frac{\Delta t_s}{m_i} \tag{22}$$

The updated positions are thus calculated using the mean values of the velocity at $r+1$th and rth time instants

$$\mathbf{x}_i^{(r+1)} = \mathbf{x}_i^{(r)} + \left(\frac{\mathbf{u}_i^{(r+1)} + \mathbf{u}_i^{(r)}}{2}\right)\ \Delta t_s \tag{23}$$

The positions of the *skin* nodes are updated in turn, using the average displacement calculated form the neighboring solid particles

$$\mathbf{x}_s^{(r+1)} = \mathbf{x}_s^{(r)} + \frac{1}{N_k}\sum_{k=1}^{N_k}\left(\mathbf{x}_k^{(r+1)} - \mathbf{x}_k^{(r)}\right) \tag{24}$$

where the subscript k is used to indicate the solid particles close to the *skin* node s.

The time step is set in order to satisfy the *Courant–Friedrichs–Lewy* condition

$$\Delta t_s <= \frac{l_{min}}{c} \tag{25}$$

where l_{min} is the length of the shortest spring and c is the wave propagation velocity which, in 3D-continuum, can be expressed as $c = \sqrt{\frac{E\ (1-\nu)}{(1+\nu)\ (1-2\nu)\ \rho_s}}$, with E corresponding to the Young's modulus, ν to the Poisson's ratio, and ρ_s to the solid density.

3.2. Fluid–structure interaction approach

As described above, in the proposed FSI approach, the fluid and the structure are represented by a finite number of particles having different physical properties and initial distance depending on the phase to which they belong. Moreover, fluid and solid computational domains are separated by interface triangles where kinematic and dynamic boundary conditions are imposed.

A bi-dimensional sketch of the two computational domains at the FSI interface is shown in Fig. 7, where the FSI triangles are discretized into line segments due to the 2D representation. The FSI interface between solid and fluid computational domains on one hand is employed to impose the hydraulic thrust to the solid domain, on the other hand is used to move the wall of the fluid computational domain under the effect of the solid deformation.

Specifically, after having updated the fluid particle velocity (Eq. (12)), the stress at the centroid $\mathbf{x}_c$ of each FSI triangle is calculated. Since the SPH method allows to obtain hydrodynamic values at the position of the internal particles, an extrapolation procedure is used to obtain wall values starting from the interior of the fluid domain. To this aim, the pressure p_c on the triangle centroid $\mathbf{x}_c$ is calculated using a Taylor series expansion carried out around the closest effective particle to $\mathbf{x}_c$ (particle A in Fig. 8a)

$$p_c = p_A\ + \sum_{j=1}^{N_A}\frac{m_j}{\rho_j}\left(p_A - p_j\right)\frac{\partial W_{A,j}}{\partial \mathbf{x}_\alpha}\ \ (\mathbf{x}_c - \mathbf{x}_A) \tag{26}$$

where $\mathbf{x}_A$ is the position of the closest particle A, N_A is the number of fluid particles lying inside the support domain of A (Ω_A), index α is defined based on the summation convention on repeated indices, $W_{A,j}$ is the kernel function considering the distance (d_{Aj}) between the particle A and its neighbor particle j.

On the other hand, the deviatoric part of the stress tensor is calculated directly on the centroid $\mathbf{x}_c$, using the velocity values of the internal fluid particles with distance shorter than kh_f from $\mathbf{x}_c$ (Fig. 8b). Specifically, by

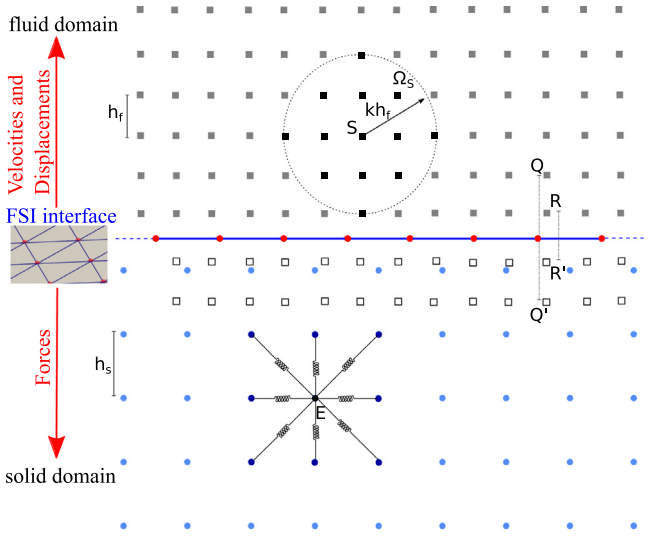

Fig. 7. 2D sketch of the fluid and solid computational domains. Gray squares: SPH fluid particles; black squares: SPH fluid particles inside the support domain (Ω_S) of the particle S; empty squares: *mirror* particles; bold blue line: FSI interface; blue and red dots: internal and *skin* nodes, respectively.

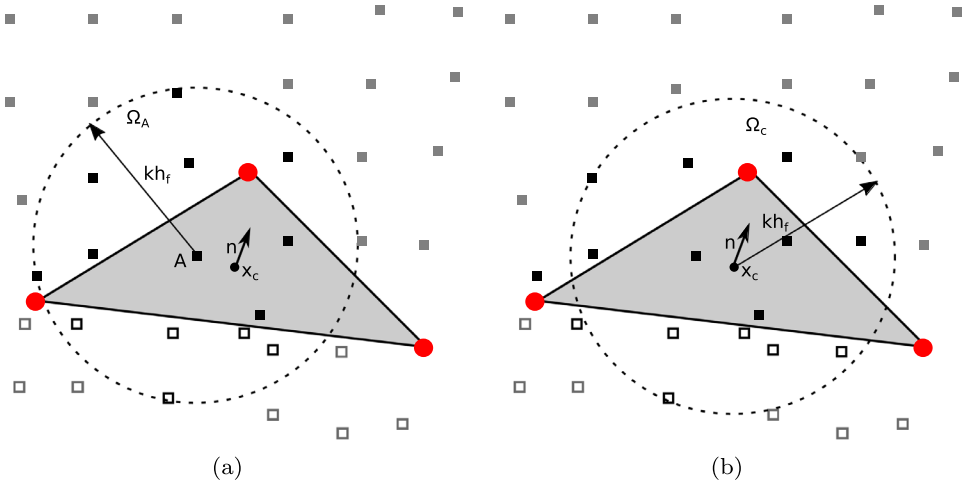

Fig. 8. Scheme of stress determination at the triangle interface. Red dots: *skin* nodes; gray squares full and empty: SPH fluid and *mirror* particles, respectively. (a) Support domain Ω_A of the closest effective particle A to the triangle centroid. Black full and empty squares: SPH fluid particle lying in Ω_A; (b) support domain Ω_c of the triangle centroid including all the internal and *mirror* fluid particles (black full and empty squares, respectively) with distance less that kh_f from $\mathbf{x}_c$.

employing the SPH *Basic Gradient Approximation* (Eq. (3)), the derivative of the α-th velocity component in the β- direction can be obtained as

$$\frac{\partial u_\alpha}{\partial x_\beta} = -\sum_{j=1}^{N_c} \frac{m_j}{\rho_j} u_{\alpha,j} \frac{\partial W_{c,j}}{\partial x_\beta} \tag{27}$$

where the sum is extended to the total number of particles N_c inside the support domain Ω_c of the triangle centroid and $W_{c,j}$ is the *kernel function* considering the distance between the point $\mathbf{x}_c$ and its neighbor internal fluid

particles j. Therefore, the stress $\boldsymbol{\sigma}_n$ on the triangle surface of normal direction $\mathbf{n}$ can be obtained as follows

$$\sigma_{n,\beta} = p_c\ n_\beta - 2\nu\rho \sum_{\alpha=1}^{3} n_\alpha \frac{\partial u_\alpha}{\partial x_\beta}\ , \text{ with } \quad \beta = 1, 2, 3 \tag{28}$$

The force exerted from the fluid domain on the FSI triangle is calculated by multiplying the stress $\boldsymbol{\sigma}_n$ by the area A_t of the triangular face. This force is equally distributed over the three *skin* nodes placed at the triangle vertices as discussed above. Thus, the force $\mathbf{f}_{ext,s}$ at each *skin* node s, which is used to define the third term of Eq. (19), is obtained as

$$\mathbf{f}_{ext,s} = \frac{1}{3} A_t\ \boldsymbol{\sigma}_n \tag{29}$$

Under the effect of the forces exerted by the fluid, the solid deforms and the *skin* nodes modify their position based on Eq. (24). This displacement is transferred to the boundaries of the fluid domain at the FSI interface. The velocity of the FSI interface is calculated at each FSI triangle averaging the velocity of the three *skin* nodes belonging to it. This velocity is then applied as boundary condition for the fluid at the FSI interface. Specifically, the component of this velocity normal to the triangular face is introduced in Eq. (10) (u_{in}^{r+1} term in the equation) as boundary condition of the PPE through the *mirror* particles generated at the FSI interface.

In general, when a partitioned approach is adopted for the simulation of FSI problems, one of the sub-domains may need substantially smaller time steps than the other, acting as a bottleneck from the solution time point of view. In this context, Hermange et al. [55] employed a SPH-FE coupled method to model violent FSI problem with a Conventional Parallel Staggered (CPS) procedure. Specifically, they adopted a SPH weakly compressible scheme which imposes very small time steps with a parallel procedure to alleviate the CPU costs coupled with an implicit FE solver. The CPS procedure assumes that, due to the very small time step of the WCSPH scheme, the fluid pressure load does not vary significantly between two consequent time instants. Since the fluid time step is typically the smallest one, the SPH solver sends its time steps and pressure loads to the FE solver and receives the structure node positions and velocities. Subsequently, both solvers evolve in time and the calculation time of fluid and solid solvers are overlapped by a synchronous updating. This CPS approach was optimized by Hermange et al. [56] to simulate tire hydroplaning on rough ground. In this version, several fluid time steps are allowed within each solid time step, and a linear extrapolation of the structure positions is performed for each fluid time step. Moreover, a check of the ratio between the fluid and solid time steps is done following the variations of the fluid loads at the end of each loop.

In the present work, although both schemes adopted for the fluid and the solid models are explicit, the Courant–Friedrichs–Lewy (CFL) condition imposed to determine the time step size yields to very different time steps for the two computational domains. In fact, due to fluid incompressibility (as discussed in Section 2.3), the velocity to be imposed in the CFL condition for this domain corresponds to the maximum fluid particle velocity, while for the solid model, which is deformable, the velocity to be considered corresponds to the wave propagation in the material (c in Eq. (25)). Therefore, being c is much higher than the maximum particle velocity, the CFL condition is necessarily more stringent in the solid model, which requires a much smaller time. Hence, in order to improve efficiency, a dual time step procedure similar to that proposed by Hermange et al. [56] is employed, where the solid phase performs multiple time steps for each time step of the fluid phase. In particular, the time step for the solid Δt_s, that satisfies Eq. (25), is selected as a fraction of Δt_f. To this aim, $\Delta t_f = n\,\Delta t_s$ with n an integer number, therefore, Eqs. (21)–(24) are solved n-times in a single fluid time step Δt_f.

A flow chart of the adopted method is shown in Fig. 9. This includes the following steps:

I. In the predictor-step, the intermediate fluid velocities are calculated (Eq. (6));
II. The PPE system is solved (Eq. (8));
III. In the corrector-step, the corrective fluid velocities are obtained (Eq. (11));
IV. The fluid particle velocities and positions are updated (Eqs. (12) (13));
V. The fluid stress on the FSI interface are calculated (Eq. (28));
VI. The fluid forces are assigned to the *skin* nodes (Eq. (29));
VII. The total forces on the solid particles are calculated (Eq. (19)) and Eq. (21) is explicitly solved employing the time step for the solid (Δt_s);

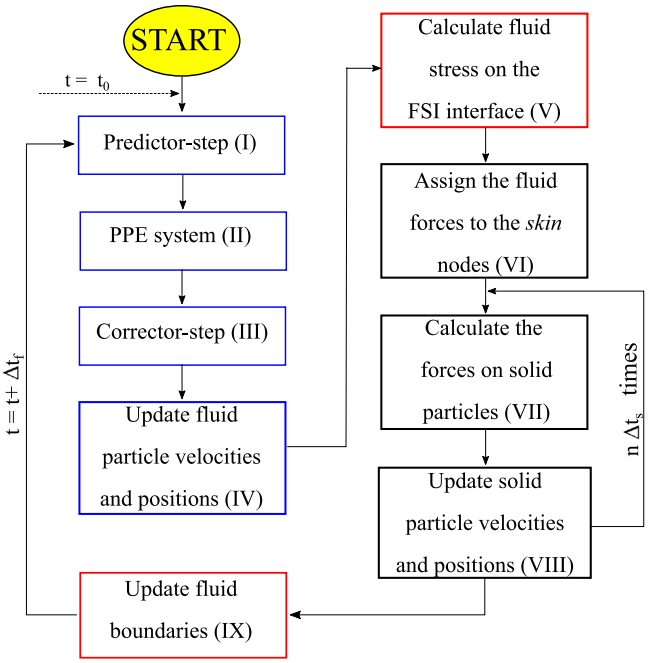

Fig. 9. Flow chart of the proposed method.

VIII. The solid particle velocities and positions are updated (Eqs. (22) and (23)), as well as the positions of the *skin* nodes (24). The procedure start again from the previous item for n times;

IX. The boundaries of the fluid domain are updated and the velocity of the FSI interface is imposed as boundary condition for the PPE (Eq. (10));

The simulation time is advanced by one fluid time step ($t = t + \Delta t_f$).

4. Determination of the spring coefficients

In this section, the procedure to obtain relations between the spring coefficients (k_e and k_v) and the material properties (Young's modulus and Poisson's ratio) is described. In particular, in Sections 4.1 and 4.2 it is demonstrated that the spring constant, k_e, is linked to the Young's modulus, E, through a factor of proportionality λ, which is independent of the geometry and particle resolution. Also, the defined spring network system results in a constant Poisson's ratio ν equal to 0.35. Section 4.3 describes how the limitation of a constant Poisson's ratio can be overcome thank to the introduction of the coefficient k_v, which imposes an additional forces on each solid particle to control the volume variation during loading. The final relations are integrated in the solid solver, which automatically computes and assigns the pair of coefficients k_e and k_v to render the requested Young's modulus and Poisson's ratio.

4.1. Analysis of the k_e spring coefficient

A solid cube of length $L = 0.01$ m (shown in Fig. 10a) is considered and a tension stress analysis is performed by imposing a constant strain $\epsilon_z = 0.5\%$ on the two cube faces of normal direction z. The two faces of the cube, of normal z, are thus moved by a quantity $\frac{1}{2}\delta_z = \frac{1}{2}\epsilon_z L$ along their positive normal direction. As discussed in Section 3.1, the displacement is transferred from the *skin* nodes lying in the two loaded faces of the cube (red dots in Fig. 10 and indicated as moving *skin* nodes in the remaining of this paper) to their neighboring solid particles (indicated as moving solid particles). The true stress is thus obtained by summing up the total force acting on the moving solid particles and dividing this force by the updated area of the two moving faces. The Young's modulus is obtained by dividing the stress by the imposed strain ϵ_z, while the Poisson's ratio is determined as the opposite of the ratio of transverse strains (ϵ_x or $\epsilon_y = \epsilon_x$ in Fig. 10b) to axial strain ϵ_z.

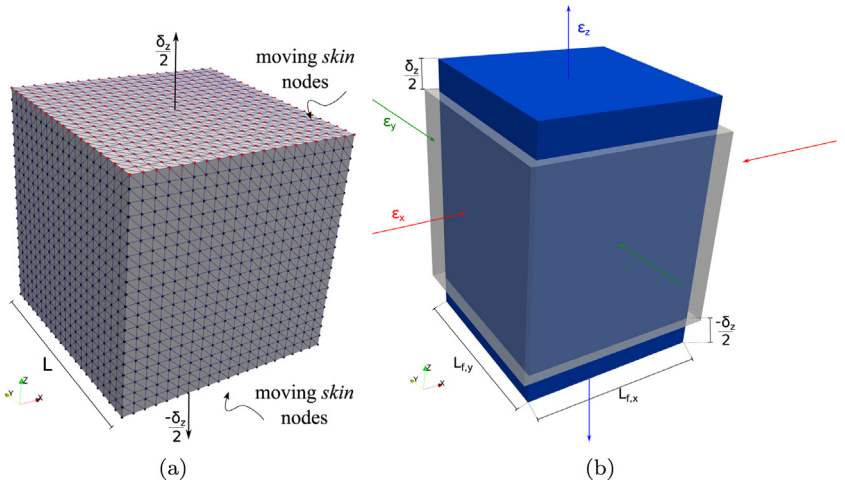

Fig. 10. (a) Cube of length $L = 0.01$. Blue lines: boundary triangles; red dots: moving *skin* nodes; black dots: *skin* nodes; (b) initial (light gray) and deformed (blue) solid geometry. The deformation in the z direction is imposed ($\epsilon_z = 0.5\%$), whilst the transversal deformations are $\epsilon_x = \frac{(L_{f,x}-L)}{L}$ and $\epsilon_y = \frac{(L_{f,y}-L)}{L}$ in the x and y-directions, respectively.

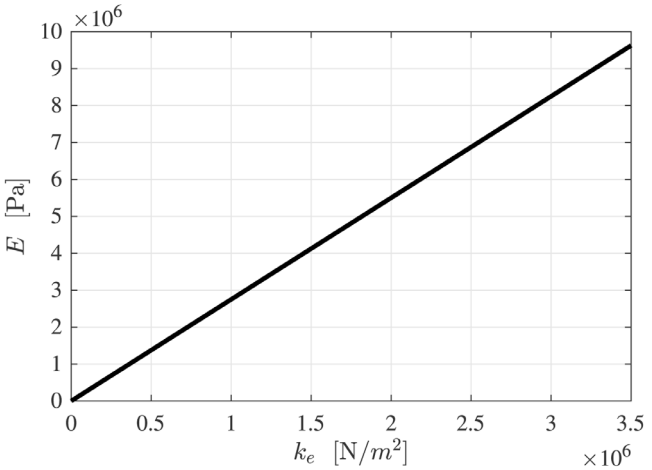

Fig. 11. Spring constant k_e and Young's modulus E with $k_v = 0$.

In this analysis, several values of k_e were used, whilst k_v was kept equal to zero, and the corresponding E and ν values were measured. The k_e values were selected equally spaced in the range of $0 \div 3500000$ to obtain a Young's modulus in the range $0 \div 10$ MPa. Results are summarized in Table 1 where some of the selected k_e coefficients are reported with the obtained Poisson's ratio, Young's modulus and ratio $\lambda = E/k_e$. The results show that, while imposing $k_v = 0$, the resulting Poisson's ratio keeps constant and is equal to $\nu = 0.35$. As shown in Fig. 11, the evolution of the Young's modulus with the spring elastic coefficient k_e is perfectly linear

$$E = \lambda\, k_e \tag{30}$$

where $\lambda = 2.75$. As discussed in Section 4.3, when the k_v coefficient is used to modify the Poisson's ratio, the parameter λ becomes a function of k_v.

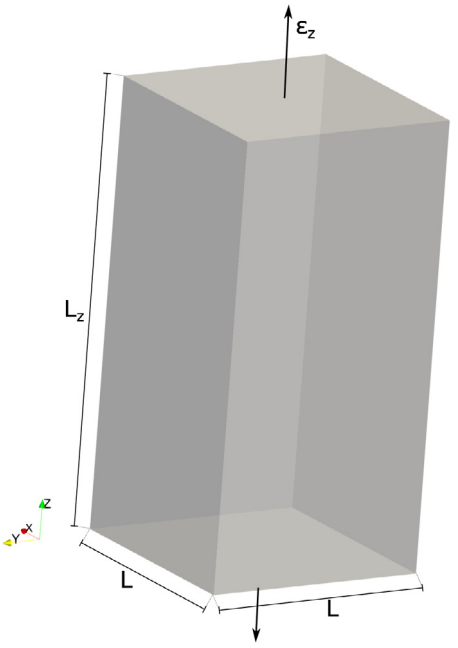

Fig. 12. Parallelepiped of base L^2 and length L_z used for the convergence analysis.

Table 1
Analysis of the Young's modulus E with the spring elastic constant k_e and Poisson's ratio with $k_v = 0$.

k_e [N/m^2]	$-\epsilon_x/\epsilon_z$ [–]	$-\epsilon_y/\epsilon_z$ [–]	E [Pa]	λ [–]
1000	0.35	0.35	2750	2.75
10 000	0.35	0.35	27 500	2.75
100 000	0.35	0.35	275 000	2.75
1 000 000	0.35	0.35	2 750 000	2.75
3 500 000	0.35	0.35	9 625 000	2.75

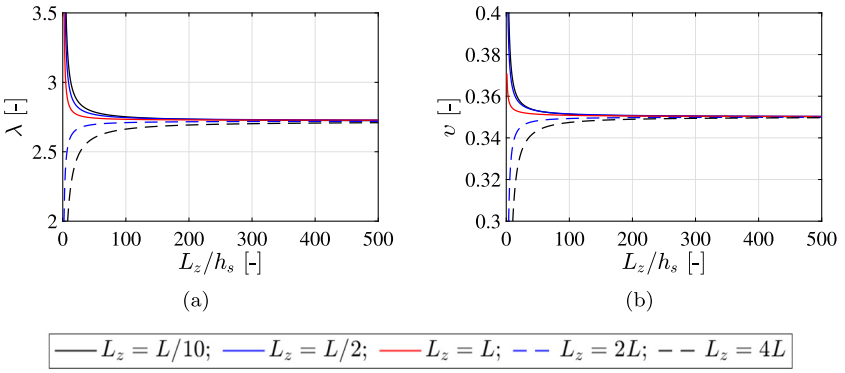

Fig. 13. Convergence analysis of the ratio $\lambda = E/k_e$ (a) and ν (b) changing the solid particle distance h_s and the length L_z. The coefficient $k_v = 0$ is zero.

4.2. Convergence analysis on the h_s parameter and on the geometry

The dependence of λ and ν on the particle distance h_s and on the geometry was investigated. To this aim, a parallelepiped with square transversal cross-section L^2 was subjected to uniaxial tensile load and analyzed for a range of axial lengths L_z varying from $L/10$ to $4L$ (see Fig. 12). Consistently with the test discussed above, a strain $\epsilon_z = 0.5\%$ was applied and the values of E and ν were obtained. Fig. 13 shows the evolution of λ and ν (Fig. 13a and b, respectively) with the number of particles along the height of the parallelepiped (L_z/h_s). In the graphs, the red lines correspond to the values obtained with $L_z = L$ (cube case). As it can be observed, for both graphs the curves having different L_z tend to a common asymptotic value equal to $\lambda = 2.73$ (Fig. 13a) and $\nu = 0.35$ (Fig. 13b).

4.3. Analysis of the k_v spring coefficient

In order to allow the selection of a specific Poisson's ratio of the material, the coefficient k_v was introduced in the analysis. Again, a cube of length L subjected to a strain $\epsilon_z = 0.5\%$ was considered. In this case, for each coefficient k_e in the range $0 \div 3\,500\,000$ (used to determine the $k_e - E$ relation in Section 4.1), the coefficient k_v was varied selecting equally spaced values in the range $-200\,000 \div 5\,500\,000$ to obtain a Poisson's ratio distribution between $0.2 \div 0.5$. As a result, two curves $k_v - \nu$ and $k_v - \lambda$ were determined. It was found that, ν and λ depend on the ratio k_v/k_e, as shown in Fig. 14. The obtained relations $\nu = f_1(k_v/k_e)$ (Fig. 14a) and $\lambda = f_2(k_v/k_e)$ (Fig. 14b) can be expressed as

$$\nu = -0.0626\ exp\left(-1.997\,\frac{k_v}{k_e}\right) - 0.08659\ exp\left(-0.4996\,\frac{k_v}{k_e}\right) + 0.4996 \tag{31}$$

$$\lambda = -0.1524\ exp\left(-1.818\,\frac{k_v}{k_e}\right) - 0.2156\ exp\left(0.2114\,\frac{k_v}{k_e}\right) + 3.111 \tag{32}$$

It should be noted that, in Eq. (30), the coefficient λ is constant for $k_v = 0$ and depends on the parameter k_v/k_e when $k_v \neq 0$.

In order to identify the pair of coefficients k_e and k_v yielding the desired value of ν and E, Eqs. (30)–(32) are integrated in the solid solver. Graphically, the procedure can be summarized as:

- The diagram in Fig. 14a is used to identify the value of k_v/k_e providing the desired value of ν;
- the graph shown in Fig. 14b is used in turn to select the coefficient λ, corresponding to the k_v/k_e previously selected;
- the k_e coefficient is obtained from Eq. (30) and used to model the required Young's modulus.

For example, a Poisson's ratio of 0.45 is highlighted in Fig. 14a which corresponds to $k_v/k_e = 1.995$ (read in the first graph) and $\lambda = 2.965$ (read in the second graph).

5. Results and discussion

5.1. Pipe deformation analysis

Womersley's deformable wall analytical solution for pulsatile flow in a cylindrical vessel [38] was employed for the validation of the FSI model. To this aim, a straight elastic cylindrical tube with internal radius $a = 5 \cdot 10^{-3}$ m and length $L = 2\,a$ was modeled (Fig. 15a). The tube wall was given a constant thickness $h = a/10 = 5 \cdot 10^{-4}$ m, which satisfies the thin-walled assumption, and was modeled as a linear elastic material with constants $E = 1$ MPa and $\nu = 0.35$. The material density was set to $\rho_s = 1100$ kg/m^3. The fluid was modeled as an incompressible Newtonian fluid with constant density $\rho_f = 1060$ kg/m^3 and dynamic viscosity $\mu = 3.5 \cdot 10^{-3}$ Pa s (similar to blood).

Fig. 15b describes the boundary conditions imposed on the fluid domain. Specifically, at the tube wall, which corresponds to the FSI interface (represented by blue triangles in Fig. 15b), the proposed FSI approach was applied (Section 3.2). The procedure described in [50] was employed to impose pressure boundary conditions for the fluid at the tube inflow and outflow cross-sections (indicated as A and B in the figure). Zero pressure was set at the

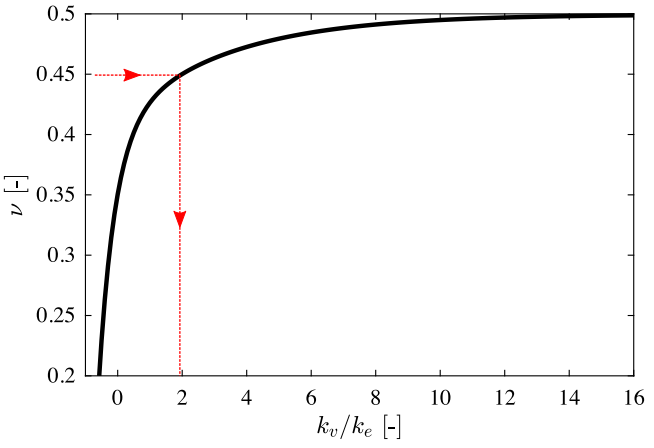

(a)

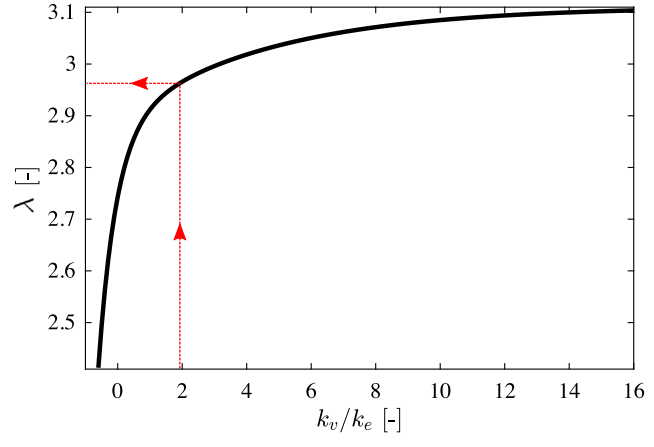

(b)

Fig. 14. (a) Poisson's ratio as function of k_v/k_e; (b) ratio between the Young's modulus and the elastic coefficient $\lambda = E/k_e$ as function of k_v/k_e.

cross-section B, whilst a uniformly distributed pressure oscillating in time was assigned at the A cross-section, by defining a sinusoidal function with period $T = 0.8$ s, angular frequency $\omega = \frac{2\pi}{T} = 7.8540$ rad/s and amplitude $P = 6$ Pa. The resulting Womersley number is equal to $Wo = a\sqrt{\frac{\omega \rho_f}{\mu}} = 7.711$. Inflow and outflow cross-sections are kept fixed in the axial direction during the simulation.

The isotropic particle initial distances were set to $h_f = 250.0 \cdot 10^{-6}$ m for the fluid and $h_s = 150.0 \cdot 10^{-6}$ m for the solid, which results in 40 SPH fluid particles along the tube internal diameter D and 3 solid particles along the tube thickness h. It should be noted that, due to the small tube thickness compared to its length, a limited number of solid particles was used along the thickness to reduce the computational efforts.

In Fig. 16 the sagittal and transversal cross-sections of the fluid and solid computational domains are shown (images on the left and on the right, respectively). In the figure, internal and *skin* nodes are represented by blue and red dots, respectively, whilst SPH fluid particles are represented by gray squares.

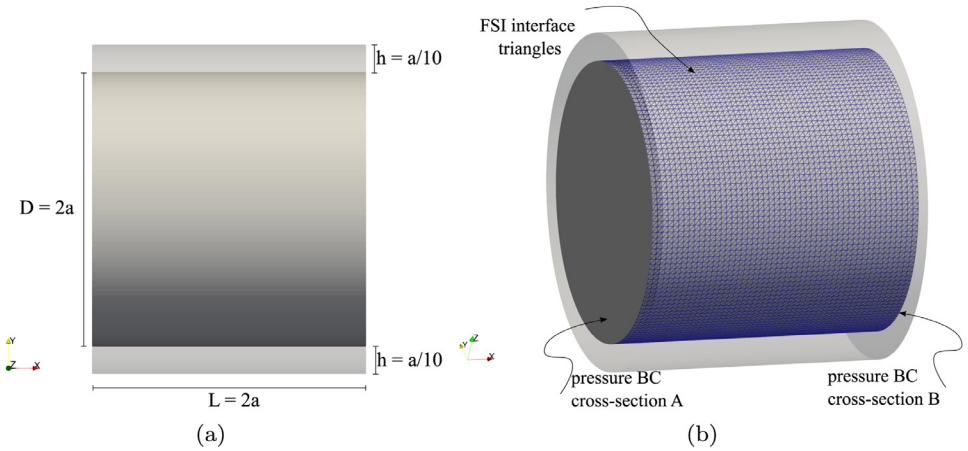

Fig. 15. (a) Tube geometry. Internal diameter $D = 2a$, length $L = 2a$, wall thickness $h = a/10$; (b) boundary conditions. Blue lines: interface FSI triangles.

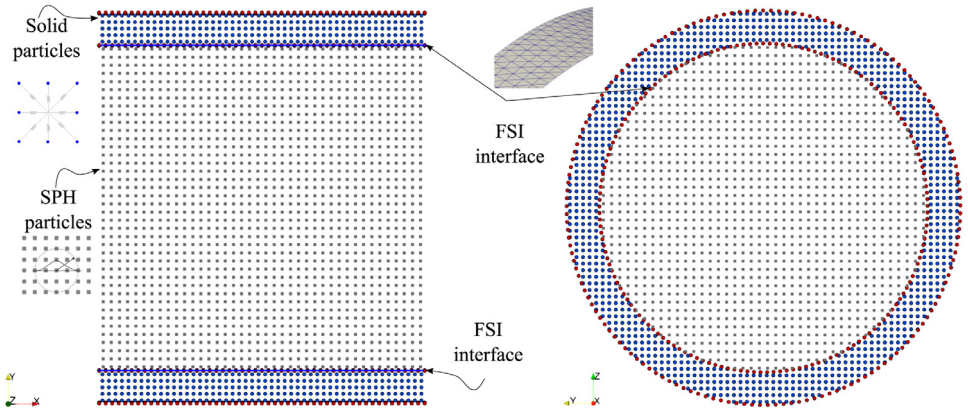

Fig. 16. Particle representation considering longitudinal and transversal sections of the tube (on the left and on the right, respectively). Gray squares: SPH fluid particles; blue and red dots: internal and *skin* nodes, respectively.

In order to write the Womersley solution in a standard form, the following three non-dimensional parameters are introduced

$$\begin{aligned} \Omega &= \sqrt{\frac{\rho_f \omega}{\mu}}\, a \\ \Lambda &= \left(\frac{i-1}{\sqrt{2}}\right) \Omega \\ \zeta &= \Lambda \frac{r}{a} \end{aligned} \tag{33}$$

In the case of a compliant tube, the change in pressure is transmitted with a finite speed. Specifically, a local increase in pressure in an elastic tube is able to locally expand the tube diameter, forming a bulge, which acts as a hydraulic compliance (accumulates and releases some of the fluid as the pressure changes). The bulge advances along the tube axis at a speed referred as the *wave speed* and indicated as c, which depends on the degree of elasticity of the tube.

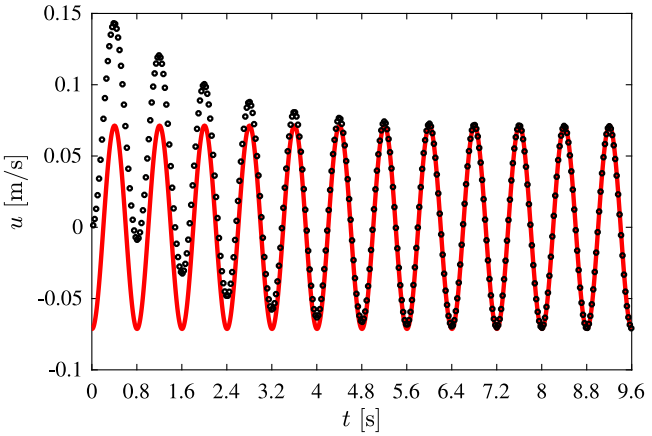

Fig. 17. Axial velocity u in the axis position ($r = 0$) at the middle section $x = L/2$. Red continuous line: analytical solution (Eq. (35)); black circles: numerical results.

The expected *wave speed* c can be determined from the wave speed equation, whose solution gives a value of c as a function of parameters of the fluid and tube wall. The wave speed equation reads as

$$\left[(g-1)(\nu^2-1)\right] z^2 + \left[\frac{\rho_s h}{\rho_f a}(g-1) + \left(2\nu - \frac{1}{2}\right) g - 2\right] z + \frac{2\rho_s h}{\rho_f a} + g = 0,$$

with

$$z = \frac{E}{1-\nu^2}\,\frac{h}{\rho_f a c^2}$$

and

$$g = \frac{2\,J_1}{\Lambda\,J_0} \tag{34}$$

where J_0 and J_1 are the Bessel functions of first kind and order zero and one, respectively. It should be noted that, in the presented test case, because of the limited length of the tube, the phenomenon can be considered as instantaneous and no phase shift of the pressure curve can be observed along the tube axis.

The analytical solution for the axial velocity u reads as

$$u\,(x, r, t) = \frac{-4\,u_s}{\Lambda^2}\left[1 - G\frac{J_0\,(\zeta)}{J_0\,(\Lambda)}\right] e^{i\omega\left(t-\frac{x}{c}\right)} \tag{35}$$

with

$$G = \frac{2 + z\,(2\nu - 1)}{z\,(2\nu - g)}$$

where G is the elasticity factor, $u_s = -\frac{k_s\,a^2}{4\mu}$ is the maximum velocity in steady flow (which is equal to 1.0714 m/s) and r is the distance along the tube radius. In Fig. 17, the velocities (black circles) at the axis ($r = 0$) at the midspan are compared with the analytical formula (red continuous line) for 14 periods. As it can be observed, the numerical results are in very good agreement with the analytical ones after 7 periods. The initial mismatching is a consequence of the numerical simulation starting from a rest configuration, while the analytical solution models a system already in its regime oscillatory pattern. Hence, few periods are needed before the analytical and numerical models become comparable.

Fig. 18 shows the velocity profiles along a tube diameter positioned at $x = L/2$, at three different time instants ($t_1 = 12\,T$, $t_2 = 12\,T + T/4$, $t_3 = 12\,T + T/2$) during the 12−th oscillation period. It should be noted that the fluid axial velocity matches the deformation rate of the solid at the wall where the kinematic coupling condition is imposed. Specifically, after calculating the loads exerted by the fluid on the solid through Eq. (28), the forces are assigned to the solid *skin* nodes (Eq. (29)). As a consequence of these forces, the solid deforms and the interface boundary triangles move accordingly.

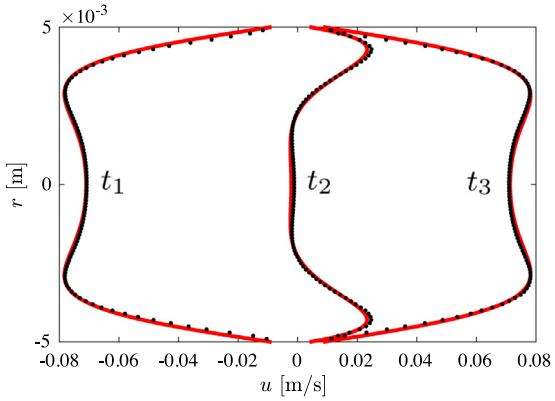

Fig. 18. Axial velocity profiles at the middle section ($x = L/2$) of the tube. Red continuous line: analytical solution (Eq. (35)); black dots: numerical results. $t_1 = 11\,T$, $t_2 = 11\,T + T/4$, $t_3 = 11\,T + T/2$.

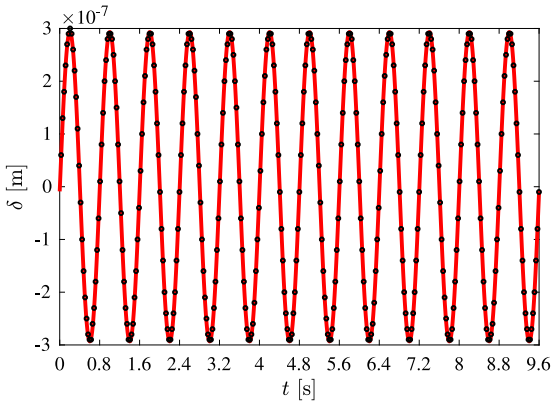

Fig. 19. Tube wall displacement at $x = 0$ as function of time. Red line: analytical solution (Eq. (36)); black circles: numerical results.

In Fig. 19, the wall radial displacement δ at the inflow cross-section was compared to the analytical solution whose equation reads as

$$\delta(x,t) = \frac{a\,P}{2\rho_f c^2}\,(1 - Gg)\,e^{i\omega\left(t-\frac{x}{c}\right)} \tag{36}$$

A good agreement between analytical and numerical results can be observed even for the radial wall displacement.

5.2. *Flow-induced vibration of an elastic beam behind a cylinder*

In this section, a canonical and challenging FSI verification problem is considered. The problem consists of a two-dimensional channel flow past a thin elastic cantilever beam attached to the lee side of a rigid circular cylinder. The present test case was initially proposed by Turek and Hron [39] and then widely adopted as benchmark for FSI solvers dealing with the presence of a deformable solid elastic structure (see, e.g., [57–59]).

A schematic of the test case with geometric dimensions and boundary conditions is shown in Fig. 20a, whilst a detail of the solid computational domain is shown in Fig. 20b. The channel has length $L = 2.5$ m and height $H = 0.41$ m. The rigid cylinder (dashed black line in Fig. 20a) has diameter $D = 0.1$ m and is centered at point $C = (2D, 2D)$, whilst the cantilever beam has length $l = 3.5D$ and thickness $b = D/5$. It should be noted that the cylinder and beam are slightly off-center with respect to the channel axis, so as to promote the onset of any physical instabilities.

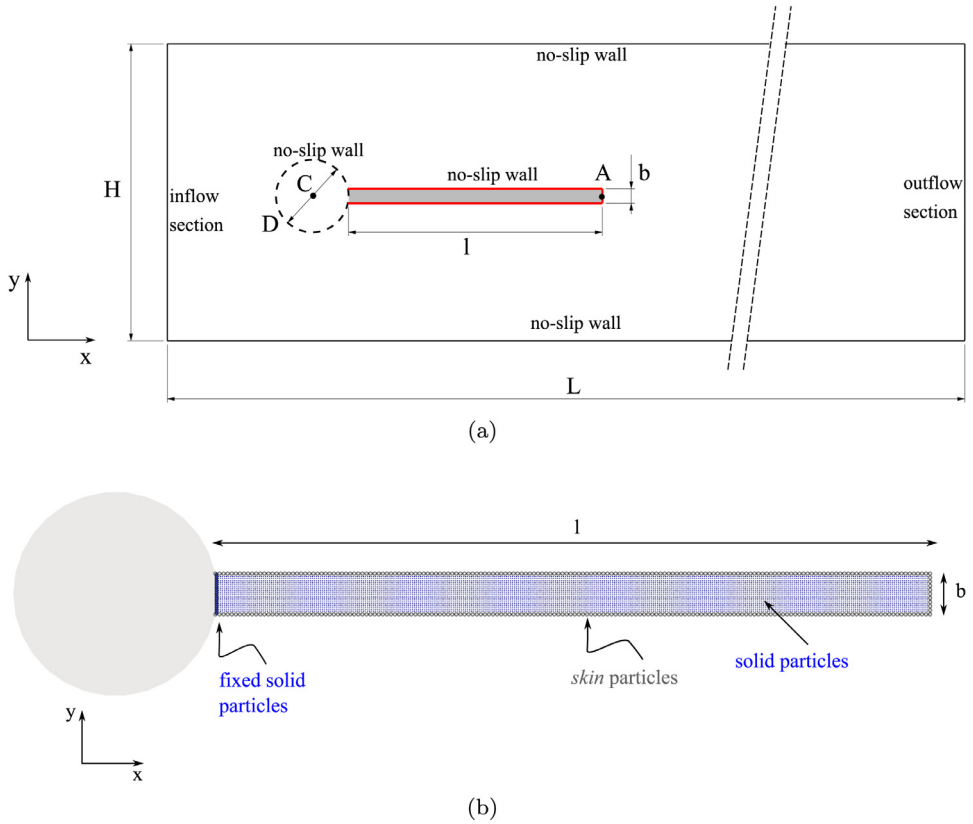

Fig. 20. (a) Sketch of the two-dimensional flow-induced vibration of a flexible beam (gray surface) attached to a rigid cylinder (dashed black line). $D = 0.1$ m, $H = 4.1D$, $l = 3.5D$, $b = D/5$, $L = 25D$. Position of the cylinder center: $C = (2D, 2D)$. Red line: FSI interface. Point A: centroid of the cross-section at the distal end of the beam structure. (b) Detail of the computational solid domain. Blue and gray points: solid particles and *skin* nodes, respectively; gray circle: rigid cylinder.

No-slip boundary condition is imposed on the top and bottom walls of the channel, on the fixed cylinder and on the fluid–structure interface separating the beam from the liquid (indicated by red lines in Fig. 20a). Inflow and outflow boundary conditions are employed at the left and right sides of the fluid domain, respectively. Specifically, at the outflow section null velocity derivatives and zero pressure are imposed, whilst at the inflow section a parabolic velocity profile is prescribed as follows

$$u(y) = 1.5\overline{u}\,\frac{y\,(H-y)}{(H/2)^2} \tag{37}$$

where $\overline{u}$ is the mean inflow velocity.

As regards the solid domain, fixed positions and velocities are imposed to the particles attached to the cylinder. These fixed particles (indicated in Fig. 20b) are included in the structure calculation, but their positions and velocities are not updated during the time integration step.

Since *PANORMUS* software is three-dimensional and, on the other hand, the test case is two-dimensional, only one layer of fluid and solid particles is simulated, imposing periodic boundary conditions on the channel faces having z-direction normal. To this aim, these periodic faces are assigned a distance equal to the particle reference distance (h_f and h_s for the fluid and solid domain, respectively). In the simulation, the solid reference distance was set to $h_s = 0.001$ m, resulting in 20 solid particles along the beam thickness ($b/h_s = 20$), whilst in the fluid domain the *smoothing length* was set to $h_f = 5\,h_s = 0.005$ m.

The so-called *FSI3* test case of Turek and Hron [39] was selected, due to its specific complexity, resulting from the combination of the model parameters: high solid deformations and equal value for the solid and fluid densities. In particular, in the *FSI3* test case, the mean inflow velocity is $\overline{u} = 2$ m/s, the Reynolds number is

Table 2
Physical parameters for *FSI3* benchmark case of Turek and Hron [39].

Parameter	Value
Fluid density (ρ_f)	1000 kg/m^3
Kinematic viscosity (ν_f)	0.001 m^2/s
Inlet mean velocity ($\overline{u}$)	2 m/s
Reynolds number (Re)	200
Structure density (ρ_s)	1000 kg/m^3
Young's modulus (E)	$5.6 \cdot 10^6$ Pa
Poisson ratio (ν)	0.4

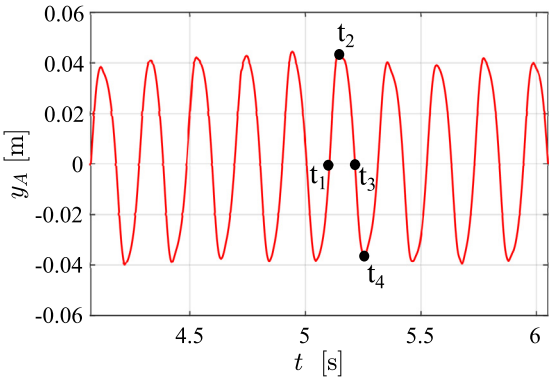

Fig. 21. Evolution in time of the vertical displacement of the point A.

$Re = \frac{\overline{u}D}{\nu_f} = 200$ and the solid and fluid densities are identical and are equal to $\rho_s = \rho_f = 1000$ kg/m^3. The fluid is modeled as incompressible and Newtonian, whereas the structure is linear elastic and compressible. A summary of the material properties for the fluid and structural domains is provided in Table 2. In order to achieve the required solid mechanical properties, relations (30)–(32) are solved imposing $\nu = 0.4$ and $E = 5.6 \cdot 10^6$ Pa. The resulting elastic constants imposed in the solid model are $k_e = 2 \cdot 10^6$ N/m^2 and $k_v = 7.89 \cdot 10^5$ N/m^2.

Fig. 21 shows a diagram of the y-coordinate $y(t)$ of the centroid of the cross-section at the distal end of the beam structure (point A) as a function of time, after reaching periodic self-sustained oscillations. The amplitude A_m and frequency f_A of the oscillation of point A in y-direction were determined and compared with literature [39,57–59]. In particular, $A_m = \frac{\delta_{max,A} - \delta_{min,A}}{2}$, with $\delta_{max,A}$ and $\delta_{min,A}$ indicating the maximum positive and negative lateral displacements of point A. Considering the average value over ten periods, the resulting amplitude and frequency of oscillation are $A_m = 0.04$ m and $f_A = 4.8$ Hz, respectively. Comparison of the obtained results with the literature, summarized in Table 3, confirms the good agreement with the results from previous studies. Also the Strouhal number $St = f_A D/\overline{u}$ was calculated (right column in Table 3), resulting in a value slightly lower than the average in the literature, although consistent with some of previous studies [59].

The snapshots of the velocity fields at four instants are shown in Fig. 22, corresponding to the extreme and intermediate deflections during the oscillation cycle of point A. To better highlight the region close to the flexible beam, only a portion of the computational domain is shown Fig. 22.

In order to highlight the vortex forming near the fluid–structure interface, an enlargement of the near beam region is shown in Fig. 23, where the velocity vectors and the beam position are represented at the same time instant as in Fig. 22.

6. Conclusions

In this study, a FSI technique has been implemented in the framework of the Lagrangian particle methods. Smoothed particle hydrodynamics method has been employed for the fluid dynamics modeling, while a simplified approach, based on particle–spring systems, has been developed for the description of the structure motion. The constants of the springs describing the solid phase mechanical response have been related to the structure mechanical

Table 3
Comparison of flapping behavior against literature. Dimensionless oscillation amplitude of the point A in y-direction (A_m/D) and Strouhal number ($St = f_A D/\overline{u}$) with f_A the frequency on oscillation of the point A.

Methods	A_m/D	St
Present	0.40	0.24
Bhardwaj and Mittal [57]	0.41	0.28
Li et al. [58]	0.41	0.26
Nestola et al. [59]	0.41	0.24
Turek and Hron [39]	0.36	0.26

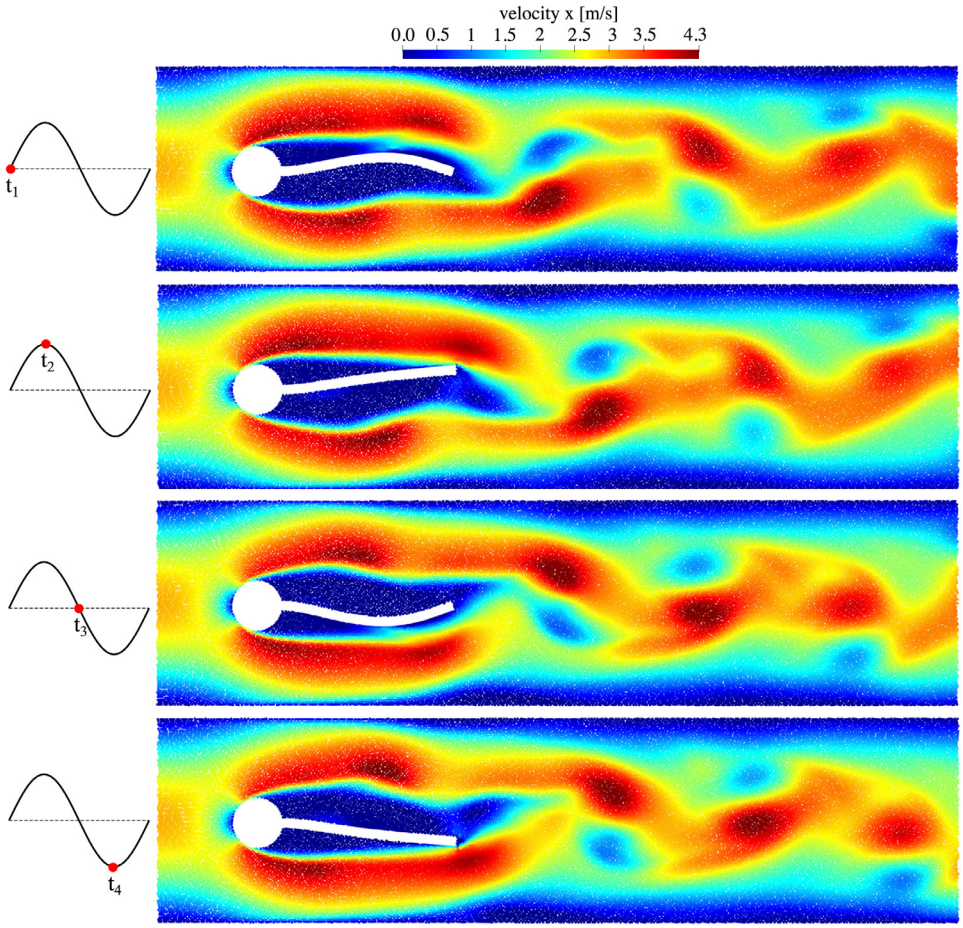

Fig. 22. Streamwise particle velocity at four time instants (indicated in Fig. 21).

properties, determining simple relationships with the Young's modulus and Poisson's ratio of the material. This feature overcomes the limitations of LSM basic schemes by allowing to set a wide range of values for the Poisson's ratio. At the interfaces separating the two computational domains, coupling conditions have been imposed to take into account the interaction of the two phases. To this aim, additional boundary particles are introduced. On one hand, the actions of the fluid on the structure are computed using an extrapolation procedure from the SPH domain, and applied as boundary conditions to the solid phase. On the other hand, as a consequence of the structure deformation, velocities and displacements of the wall are imposed to the fluid domain through the mirror particle procedure. This procedure naturally avoids the penetration of fluid particles into the solid domain. Numerical results

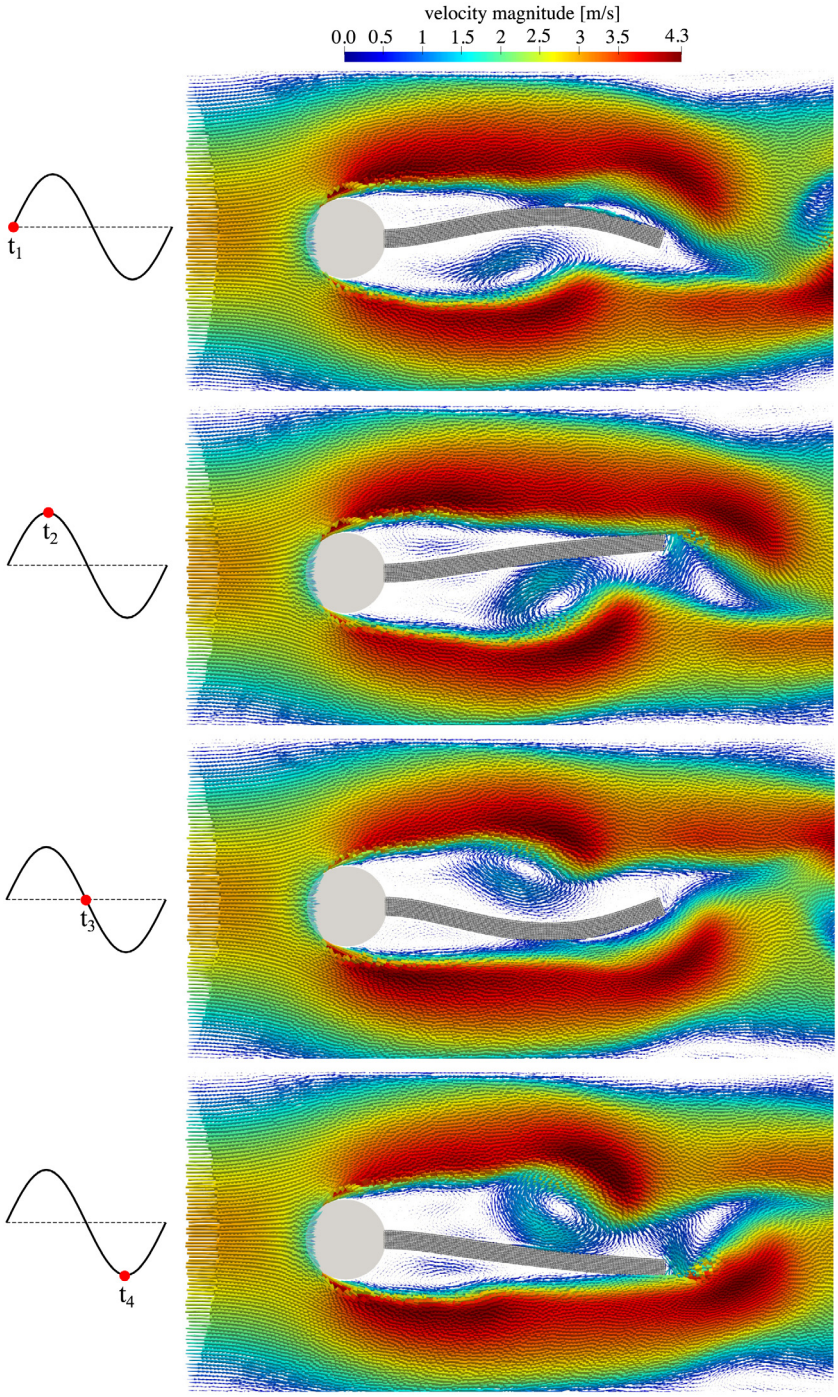

Fig. 23. Velocity vectors and beam position at four time instants (indicated in Fig. 21).

are in good agreement with the Womersley's analytical solutions and the benchmark test proposed by Turek and Hron [39].

Of course, there are several limitations within the proposed discrete solid model. In particular, as the methodology is mainly aimed at modeling the fluid dynamics, advantage was taken of the simplicity of a particle–spring model

for the solid phase description. This, at this stage, does not model the complex non-linear constitutive behavior characterizing soft tissues, nor their anisotropic behavior. However, the method has shown to be very versatile and suitable to easily incorporate more complex constitutive models.

On the other hand, an important advantage of the proposed FSI method is that the spatial–temporal discretization of the fluid and solid are not related, allowing to optimize the computational efficiency by refining each domain based on the specific case.

In conclusion, the proposed approach is suitable to be expanded to the modeling of crucial solid–liquid problems typical of cardiovascular studies such as the dynamics of cardiovascular valves, or the formation, growth and behavior of thrombi and plaques interacting with the blood flow. In this framework, such FSI analysis based on particle model could become a versatile tool supporting the understanding of complex physiological phenomena and the development of new therapeutic solutions.

Declaration of competing interest

The authors declare that they have no known competing financial interests or personal relationships that could have appeared to influence the work reported in this paper.

Funding

This work was supported by the Programme Patto per il Sud Regione Sicilia, Italy - FSC 2014/2020 (Project Computational Molecular Design and Screening CHeMISt).

Appendix A. Supplementary data

Supplementary material related to this article can be found online at https://doi.org/10.1016/j.cma.2022.114728.

References

[1] C. Farhat, M. Lesoinne, Two efficient staggered algorithms for the serial and parallel solution of three-dimensional nonlinear transient aeroelastic problems, Comput. Methods Appl. Mech. Engrg. 182 (3–4) (2000) 499–515.
[2] M. Souli, A. Ouahsine, L. Lewin, Ale formulation for fluid–structure interaction problems, Comput. Methods Appl. Mech. Engrg. 190 (5–7) (2000) 659–675.
[3] E. Kuhl, S. Hulshoff, R. De Borst, An arbitrary Lagrangian Eulerian finite-element approach for fluid–structure interaction phenomena, Int. J. Numer. Methods Eng. 57 (1) (2003) 117–142.
[4] G. Lipari, E. Napoli, The impacts of the ALE and hydrostatic-pressure approaches on the energy budget of unsteady free-surface flows, Comput. & Fluids 37 (6) (2008) 656–673.
[5] C.S. Peskin, The immersed boundary method, Acta Numer. 11 (2002) 479–517.
[6] S.R. Idelsohn, J. Marti, A. Limache, E. Oñate, Unified Lagrangian formulation for elastic solids and incompressible fluids: application to fluid–structure interaction problems via the PFEM, Comput. Methods Appl. Mech. Engrg. 197 (19–20) (2008) 1762–1776.
[7] P. Ryzhakov, R. Rossi, S. Idelsohn, E. Onate, A monolithic Lagrangian approach for fluid–structure interaction problems, Comput. Mech. 46 (6) (2010) 883–899.
[8] A. Franci, E. Oñate, J.M. Carbonell, Unified Lagrangian formulation for solid and fluid mechanics and FSI problems, Comput. Methods Appl. Mech. Engrg. 298 (2016) 520–547.
[9] M.L. Cerquaglia, D. Thomas, R. Boman, V. Terrapon, J.-P. Ponthot, A fully partitioned Lagrangian framework for FSI problems characterized by free surfaces, large solid deformations and displacements, and strong added-mass effects, Comput. Methods Appl. Mech. Engrg. 348 (2019) 409–442.
[10] M. Liu, G. Liu, Smoothed particle hydrodynamics (SPH): an overview and recent developments, Arch. Comput. Methods Eng. 17 (1) (2010) 25–76.
[11] L.B. Lucy, A numerical approach to the testing of the fission hypothesis, Astron. J. 82 (1977) 1013–1024.
[12] R.A. Gingold, J.J. Monaghan, Smoothed particle hydrodynamics: theory and application to non-spherical stars, Mon. Not. R. Astron. Soc. 181 (3) (1977) 375–389.
[13] J.J. Monaghan, Smoothed particle hydrodynamics and its diverse applications, Annu. Rev. Fluid Mech. 44 (2012) 323–346.
[14] M. Liu, Z. Zhang, Smoothed particle hydrodynamics (SPH) for modeling fluid-structure interactions, Sci. China Phys. Mech. Astron. 62 (8) (2019) 984701.
[15] T. De Vuyst, R. Vignjevic, J. Campbell, Coupling between meshless and finite element methods, Int. J. Impact Eng. 31 (8) (2005) 1054–1064.
[16] P.H. Groenenboom, B.K. Cartwright, Hydrodynamics and fluid-structure interaction by coupled SPH-FE method, J. Hydraul. Res. 48 (sup1) (2010) 61–73.

[17] Z. Li, J. Leduc, A. Combescure, F. Leboeuf, Coupling of SPH-ALE method and finite element method for transient fluid–structure interaction, Comput. & Fluids 103 (2014) 6–17.
[18] Z. Li, J. Leduc, J. Nunez-Ramirez, A. Combescure, J.-C. Marongiu, A non-intrusive partitioned approach to couple smoothed particle hydrodynamics and finite element methods for transient fluid-structure interaction problems with large interface motion, Comput. Mech. 55 (4) (2015) 697–718.
[19] B. Serván-Camas, J. Cercós-Pita, J. Colom-Cobb, J. García-Espinosa, A. Souto-Iglesias, Time domain simulation of coupled sloshing–seakeeping problems by SPH–FEM coupling, Ocean Eng. 123 (2016) 383–396.
[20] G. Fourey, C. Hermange, D. Le Touzé, G. Oger, An efficient FSI coupling strategy between smoothed particle hydrodynamics and finite element methods, Comput. Phys. Comm. 217 (2017) 66–81.
[21] T. Long, D. Hu, D. Wan, C. Zhuang, G. Yang, An arbitrary boundary with ghost particles incorporated in coupled FEM–SPH model for FSI problems, J. Comput. Phys. 350 (2017) 166–183.
[22] P. Sun, D. Le Touzé, A.-M. Zhang, Study of a complex fluid-structure dam-breaking benchmark problem using a multi-phase SPH method with APR, Eng. Anal. Bound. Elem. 104 (2019) 240–258.
[23] S.M. Hosseini, J.J. Feng, A particle-based model for the transport of erythrocytes in capillaries, Chem. Eng. Sci. 64 (22) (2009) 4488–4497.
[24] X. Yang, M. Liu, S. Peng, C. Huang, Numerical modeling of dam-break flow impacting on flexible structures using an improved SPH–EBG method, Coast. Eng. 108 (2016) 56–64.
[25] C. Antoci, M. Gallati, S. Sibilla, Numerical simulation of fluid–structure interaction by SPH, Comput. Struct. 85 (11–14) (2007) 879–890.
[26] C. Zhang, M. Rezavand, X. Hu, A multi-resolution SPH method for fluid-structure interactions, J. Comput. Phys. 429 (2021) 110028.
[27] A. Rafiee, K.P. Thiagarajan, An SPH projection method for simulating fluid-hypoelastic structure interaction, Comput. Methods Appl. Mech. Engrg. 198 (33–36) (2009) 2785–2795.
[28] A. Khayyer, H. Gotoh, H. Falahaty, Y. Shimizu, An enhanced ISPH–SPH coupled method for simulation of incompressible fluid–elastic structure interactions, Comput. Phys. Comm. 232 (2018) 139–164.
[29] D.S. Morikawa, M. Asai, Coupling total Lagrangian SPH–EISPH for fluid–structure interaction with large deformed hyperelastic solid bodies, Comput. Methods Appl. Mech. Engrg. 381 (2021) 113832.
[30] C.H. Lee, A.J. Gil, G. Greto, S. Kulasegaram, J. Bonet, A new Jameson–Schmidt–Turkel smooth particle hydrodynamics algorithm for large strain explicit fast dynamics, Comput. Methods Appl. Mech. Engrg. 311 (2016) 71–111.
[31] D. Barcarolo, D. Le Touzé, F. de Vuyst, Validation of a new fully-explicit incompressible smoothed particle hydrodynamics method, Blucher Mech. Eng. Proc. 1 (1) (2014).
[32] G.A. Buxton, R. Verberg, D. Jasnow, A.C. Balazs, Newtonian fluid meets an elastic solid: coupling lattice Boltzmann and lattice-spring models, Phys. Rev. E 71 (5) (2005) 056707.
[33] H. Tan, S. Chen, A hybrid DEM-sph model for deformable landslide and its generated surge waves, Adv. Water Resour. 108 (2017) 256–276.
[34] K. Wu, D. Yang, N. Wright, A coupled SPH-DEM model for fluid-structure interaction problems with free-surface flow and structural failure, Comput. Struct. 177 (2016) 141–161.
[35] M. Ariane, D. Vigolo, A. Brill, F. Nash, M. Barigou, A. Alexiadis, Using discrete multi-physics for studying the dynamics of emboli in flexible venous valves, Comput. & Fluids 166 (2018) 57–63.
[36] K. Ng, A. Alexiadis, H. Chen, T. Sheu, A coupled smoothed particle hydrodynamics-volume compensated particle method (SPH-VCPM) for fluid structure interaction (FSI) modelling, Ocean Eng. 218 (2020) 107923.
[37] J. O'Connor, B.D. Rogers, A fluid–structure interaction model for free-surface flows and flexible structures using smoothed particle hydrodynamics on a GPU, J. Fluids Struct. 104 (2021) 103312.
[38] J.R. Womersley, XxIV. Oscillatory motion of a viscous liquid in a thin-walled elastic tube—I: The linear approximation for long waves, Lond. Edinb. Dublin Philos. Mag. J. Sci. 46 (373) (1955) 199–221.
[39] S. Turek, J. Hron, Proposal for numerical benchmarking of fluid-structure interaction between an elastic object and laminar incompressible flow, in: Fluid-Structure Interaction, Springer, 2006, pp. 371–385.
[40] E. Napoli, PANORMUS User's manual, University of Palermo, Palermo, Italy, 2011, pp. 1–74.
[41] E. Napoli, M. De Marchis, E. Vitanza, PANORMUS-SPH. a new smoothed particle hydrodynamics solver for incompressible flows, Comput. & Fluids 106 (2015) 185–195.
[42] H. Wendland, Piecewise polynomial, positive definite and compactly supported radial functions of minimal degree, Adv. Comput. Math. 4 (1) (1995) 389–396.
[43] A. Colagrossi, M. Landrini, Numerical simulation of interfacial flows by smoothed particle hydrodynamics, J. Comput. Phys. 191 (2) (2003) 448–475.
[44] G. Oger, M. Doring, B. Alessandrini, P. Ferrant, An improved SPH method: Towards higher order convergence, J. Comput. Phys. 225 (2) (2007) 1472–1492.
[45] S. Marrone, M. Antuono, A. Colagrossi, G. Colicchio, D. Le Touzé, G. Graziani, δ-SPH model for simulating violent impact flows, Comput. Methods Appl. Mech. Engrg. 200 (13–16) (2011) 1526–1542.
[46] S.J. Lind, R. Xu, P.K. Stansby, B.D. Rogers, Incompressible smoothed particle hydrodynamics for free-surface flows: A generalised diffusion-based algorithm for stability and validations for impulsive flows and propagating waves, J. Comput. Phys. 231 (4) (2012) 1499–1523.
[47] B. Bouscasse, A. Colagrossi, S. Marrone, M. Antuono, Nonlinear water wave interaction with floating bodies in SPH, J. Fluids Struct. 42 (2013) 112–129.

[48] A. Skillen, S. Lind, P.K. Stansby, B.D. Rogers, Incompressible smoothed particle hydrodynamics (SPH) with reduced temporal noise and generalised fickian smoothing applied to body–water slam and efficient wave–body interaction, Comput. Methods Appl. Mech. Engrg. 265 (2013) 163–173.
[49] E. Napoli, M. De Marchis, C. Gianguzzi, B. Milici, A. Monteleone, A coupled finite volume–smoothed particle hydrodynamics method for incompressible flows, Comput. Methods Appl. Mech. Engrg. 310 (2016) 674–693.
[50] A. Monteleone, M. Monteforte, E. Napoli, Inflow/outflow pressure boundary conditions for smoothed particle hydrodynamics simulations of incompressible flows, Comput. & Fluids 159 (2017) 9–22.
[51] A. Monteleone, M. De Marchis, B. Milici, E. Napoli, A multi-domain approach for smoothed particle hydrodynamics simulations of highly complex flows, Comput. Methods Appl. Mech. Engrg. 340 (2018) 956–977.
[52] J.P. Morris, P.J. Fox, Y. Zhu, Modeling low Reynolds number incompressible flows using SPH, J. Comput. Phys. 136 (1) (1997) 214–226.
[53] Y. Zang, R.L. Street, J.R. Koseff, A non-staggered grid, fractional step method for time-dependent incompressible Navier-Stokes equations in curvilinear coordinates, J. Comput. Phys. 114 (1) (1994) 18–33.
[54] H.A. Van der Vorst, Bi-CGSTAB: A fast and smoothly converging variant of Bi-CG for the solution of nonsymmetric linear systems, SIAM J. Sci. Statist. Comput. 13 (2) (1992) 631–644.
[55] C. Hermange, G. Oger, D. Le Touzé, Energy considerations in the SPH method with deformable boundaries and application to FSI problems, J. Comput. Phys.: X 1 (2019) 100008.
[56] C. Hermange, G. Oger, Y. Le Chenadec, D. Le Touzé, A 3D SPH–FE coupling for FSI problems and its application to tire hydroplaning simulations on rough ground, Comput. Methods Appl. Mech. Engrg. 355 (2019) 558–590.
[57] R. Bhardwaj, R. Mittal, Benchmarking a coupled immersed-boundary-finite-element solver for large-scale flow-induced deformation, AIAA J. 50 (7) (2012) 1638–1642.
[58] Z. Li, W. Cao, D. Le Touzé, On the coupling of a direct-forcing immersed boundary method and the regularized lattice Boltzmann method for fluid-structure interaction, Comput. & Fluids 190 (2019) 470–484.
[59] M.G.C. Nestola, B. Becsek, H. Zolfaghari, P. Zulian, D. De Marinis, R. Krause, D. Obrist, An immersed boundary method for fluid-structure interaction based on variational transfer, J. Comput. Phys. 398 (2019) 108884.